Reanalysis of the ^{13}N$(p, \gamma)^{14}$O reaction and its role in the stellar CNO cycle

S. B. Dubovichenko [1,2] R. Ya. Kezerashvili [3,4] N. A. Burkova,[2] A. V. Dzhazairov-Kakhramanov [1] and B. Beisenov[1,2]

^{1}*Fesenkov Astrophysical Institute "NCSRT" ASA MDASI RK, 050020, Almaty, Kazakhstan*
^{2}*al-Farabi Kazakh National University, 050040, Almaty, Kazakhstan*
^{3}*New York City College of Technology, City University of New York, Brooklyn, New York 11201, USA*
^{4}*Graduate School and University Center, City University of New York, New York 10016, USA*

Within the framework of the modified potential cluster model with forbidden states, the ^{13}N$(p, \gamma)^{14}$O reaction rate and the astrophysical S factor are considered. It is shown that the first p^{13}N resonance determines the S factor and contributions of the $M1$ and $E2$ transitions are negligible at energies $E < 1$ MeV, but are significant at high energies. The S factor strongly depends on the $^3S_1$ resonance parameters. The influence of the width of the $^3S_1$ resonance on the S factor is demonstrated. The reaction rate is calculated and an analytical approximation for the reaction rate is proposed. A comparison of our calculation with existing data is addressed. Results of our calculations for the ^{13}N$(p, \gamma)^{14}$O reaction rate provide the contribution to the steadily improving reaction-rate database libraries. Our calculations of the ^{13}N$(p, \gamma)^{14}$O reaction rate along with results for the rates of the ^{14}N$(p, \gamma)^{15}$O and ^{12}C$(p, \gamma)^{13}$N processes provide the temperature range $0.13 < T_9 < 0.97$ for the conversion of the carbon-nitrogen-oxygen (CNO) cycle to the hot CNO cycle. Our results demonstrate that, at the early stages of a nova explosion at temperatures of about $0.1T_9$ and at late stages of evolution of supermassive stars at temperatures of about $1.0T_9$, the ignition of the hot CNO cycle could occur at much lower densities of a stellar medium.

I. INTRODUCTION

Radiative capture reactions play an important role in astrophysics. Light elements are either created during the big bang or during fusion reactions in stars. In the latter case, they are the result of hydrogen burning, which is characterized by two major reaction sequences: (i) the pp chain, and (ii) the carbon-nitrogen-oxygen (CNO) cycle [1]. The CNO cycle is considered as a catalytic process that requires the presence of some initial carbon, nitrogen, and oxygen abundance in the stellar material. Radiative capture reactions, namely those in which an atomic nucleus fuses with one proton or neutron and produces a nucleus with the emission of electromagnetic radiation, or with α-particle emission, have the greatest importance in nuclear astrophysics [2,3]. In particular, competing (p, γ) and (p, α) reactions are branching points in the CNO cycling process [1]. However, the strong-interaction (p, α) branch is substantially stronger than the electromagnetic (p, γ) branch, but, in some cases, the latter one can be comparable with the (p, α), which alters the reaction flow substantially in certain astrophysical temperature regimes [4]. The proton-induced radiative capture reactions (p, γ) occur in many stellar environments, for example, in novae and x-ray bursts. Especially in stellar environments due to the high temperatures and short reaction times, (p, γ) reactions involving short-lived nuclei play an important role for energy generation and nucleosynthesis. It takes the high-density environment of stars to generate nuclei with masses

$A \geqslant 12$. The reactions of protons' radiative capture are widely discussed in the literature (see reviews [2,3,5] and references therein). It is done primarily due to the fact that the carbon component burns out in a series of processes known as the hot CNO cycle (HCNO-I), which occurs at temperatures starting from $0.2T_9$ [1]. The synthesized isotope ^{14}O is considered as a waiting point, which is overcome by a chain of reactions, starting with ^{14}O$(\alpha, p)^{17}$F when temperature is above $0.4T_9$. The review [1] presents comprehensive and consistent illustrations of CNO and HCNO-I cycle chains, as well as the evolution of the CNO isotope abundance with time for different density and temperature conditions, the calculations of which are directly based on the reaction rates.

The pioneering measurement with a rare-isotope beam was the first direct determination of the ^{13}N$(p, \gamma)^{14}$O reaction cross section using a radioactive ^{13}N beam [6–8]. In the reaction ^{13}N$(p, \gamma)^{14}$O the s-wave capture on the broad 1^- resonance dominates the reaction rate and, over three decades, many efforts have been made to determine the parameters for resonance using different experimental approaches: transfer reactions [7,9–11], Coulomb dissociation of a high energy ^{14}O beam in the field of a heavy nucleus [12–14], a rare-isotope beam [6–8], the use of the unstable ion beam by indirect measurements [15,16], and, most recently, via neutron-knockout reactions with a fast ^{15}O beam [17]. Reference [5] provides an overview of current experimental projects specializing in the synthesis of radioactive isotope beams and experiments on astrophysical applications. However, there is no

experimental data today suitable for comparison with theoretical calculations of cross sections or astrophysical S factors. In this case, apparently, it is possible to synthesize ^{13}N isotope beams, given that its lifetime of 9.965 min is comparable with the neutron lifetime. At the same time, direct measurements of the ^{14}O(α, p) ^{17}F reaction are carried out, although the β^+ decay of isotope ^{14}O is 70.598 s. Nevertheless, in the future we can expect new data for cross sections of the process ^{13}N(p, γ) ^{14}O [5].

The results of the studies [6,8,15,16,18–24] on astrophysical S factor and ^{13}N(p, γ) ^{14}O reaction rate are included in the nuclear astrophysics compilation of reactions (NACRE) database [25] and in the new compilation, referred to as NACRE II [26]. These databases form the basis for macroscopic astrophysical calculations. The key generalizing element of all calculations is the first $^3S_1$ resonance in the p ^{13}N scattering channel, and all calculations are based on the energy and the width of this resonance. In the above-mentioned works, experimental data on these characteristics are taken from Ajzenberg's 1991 compilation [27]. At present, new data are available on the spectra of the ^{14}O nucleus [28]. Therefore, it is relevant to consider these data for analysis of the ^{13}N(p, γ) ^{14}O reaction. Moreover, another incentive for these calculations are the data from the latest experimental research [17] that will also be brought to our discussion.

Theoretical calculations of a reaction rate rely on the reaction cross section, which is determined by the nuclear structure of the nuclei involved, the reaction mechanism, and the associated interaction forces. The cross section can be calculated in the framework of *ab initio* models, where it is determined by using the wave functions (WFs) of the system, but subject to uncertainties associated with the theoretical model and the quality of the optical potential. Most notable are cluster model approaches, where nucleons are grouped in clusters of particles, which is a configuration that might, in particular, enhance the reaction rates and that also rely on the quality of the optical potential [29–31]. Calculations of the rate for the ^{13}N(p, γ) ^{14}O reaction and the astrophysical S factor were performed within potential models using shell-model, cluster-model, and R-matrix approaches [18–20,22,23]. There are significant differences between the various calculations of the ^{13}N(p, γ) ^{14}O reaction and, in light of a new experimental study [17], an independent and well-established approach is greatly needed to analyze this process. Continuing our studies of the processes of radiative capture on light atomic nuclei (see Refs. [29,31–33] for concise summaries), we consider the reaction of $p + {}^{13}$N $\rightarrow {}^{14}$O $+ \gamma$ at astrophysical energies. This process is clearly not included in the thermonuclear standard CNO cycle, but it makes a certain contribution to accumulation processes of a stable ^{14}N nucleus, which is further involved in other reactions of this cycle [34] and belongs to the hot CNO cycle [1].

The goal of this study is twofold: (i) to calculate the cross section of the ^{13}N(p, γ) ^{14}O reaction at the energies of astrophysical interest and the reaction rate as a function of temperature for the analyses of the influence of the first p ^{13}N resonance width on the astrophysical S factor; and (ii) to analyze and determine a temperature range for the conversion of the CNO cycle to the HCNO cycle.

The article is organized as follows: In Sec. II the potential cluster model with the classification of orbital states and methods of calculations are described. Classification and structure of states are introduced and analyzed in Sec. III, while in Sec. IV the potentials for the p ^{13}N interaction are presented. Astrophysical S factors of the proton radiative capture on ^{13}N and the ^{13}N(p, γ) ^{14}O reaction rate are given in Sec. V. The role of the ^{13}N(p, γ) ^{14}O reaction in the conversion from the CNO to the hot CNO cycle is discussed in Sec. VI. Conclusions follow in Sec. VII.

II. THEORETICAL MODEL AND FORMALISM

To carry out calculations of astrophysical S factors for various reactions, we usually use the modified potential cluster model (MPCM) of light atomic nuclei [29,31–33,35] with the classification of orbital states according to Young diagrams [36,37]. The model provides relatively many simple possibilities for performing calculations of various astrophysical characteristics. For example, one can calculate the astrophysical S factor of radiative capture for electromagnetic transitions from scattering states of clusters to bound states (BSs) of light atomic nuclei in cluster channels [29,31]. The choice of this model is due to the fact that, in many atomic nuclei, the probability of cluster formation and the degree of their separation are relatively high. This is confirmed by numerous experimental data and various theoretical calculations obtained in various works over the past few decades [37].

Thermonuclear rates are defined by reaction cross sections that can be obtained by using a theoretical model. In the present study of the ^{13}N(p, γ) ^{14}O reaction we use the modified potential cluster model, where a proton interacts with a system of nucleons which are grouped into cluster ^{13}N. States of the p-^{13}N system are defined by the classification according to Young diagrams. Relative motion WFs are determined by solving the Schrödinger equation [29,31,32,35]. The entry channel presents the proton $p(\frac{1}{2}^+)$ (J^π is the total momentum and parity) and ^{13}N$(\frac{1}{2}^-)$ nucleus. For description of the final state we assume that ^{14}O nucleus consist of the same particles as in the initial channel, but in the bound state.

In the microscopic formalism widely known as the resonating-group method [38,39], the wave function (WF) of the p ^{13}N system has the form of an antisymmetrized product of internal cluster wave functions and a WF of their relative motion:

$$\Psi = \hat{A}[\psi_p(\mathbf{r}_1)\psi_{^{13}N}(\mathbf{r}_2)\chi(\mathbf{r}_1 - \mathbf{r}_2)]. \quad (1)$$

In Eq. (1) $\hat{A}$ is the antisymmetrization operator, $\psi_p(\mathbf{r}_1)$ and $\psi_{^{13}N}(\mathbf{r}_2)$ are the wave functions of the proton and ^{13}N nucleus, respectively, $\mathbf{r}_1$ and $\mathbf{r}_2$ are the radius vectors of their center of mass, $\chi(\mathbf{r})$ is the WF of their relative motion, while $\mathbf{r} = \mathbf{r}_1 - \mathbf{r}_2$.

According to Refs. [36,38] the WF of ^{13}N is antisymmetrized. Thus, only exchange transpositions between nucleons of the ^{13}N nucleus and proton must be taken into account, which leads to the modification of the function. By contrast, in our approach this method of antisymmetrization consists in the effective accounting of the Pauli principle

by using the deep attractive potentials with the forbidden states (FSs). Mathematically, this realization is based on the classification of orbital states according to the Young diagrams [36,37]. Exclusion of FSs from spectra leads to the correct node behavior of the function in the internal range, both for a bound state and for a continuous spectrum that, in its turn, reflects on the asymptotics of these functions.

To build interaction potentials between the proton and ^{13}N for scattering states in the MPCM, results of phase shift analysis of experimental data of differential cross sections for an elastic scattering of corresponding particles are generally used. The other way to build the potentials is to use spectra of the resulting nucleus ^{14}O [29,31]. Moreover, the multiparticle nature of the problem is taken into account by dividing single-particle levels of such a potential into states allowed and forbidden by the Pauli principle [36,37]. The concept of Pauli-forbidden states allows one to consider the multibody character of the problem in terms of two-body interaction potential between clusters. Potentials for bound states (BSs) of p and ^{13}N particles are built primarily based on the requirement to describe the main characteristics of the ^{14}O nucleus. For example, this is a requirement to reproduce the binding energy of ^{14}O in a corresponding $p\,^{13}$N cluster channel and a description of the other static nuclear characteristics, such as a charge radius and asymptotic constant (AC), with the same potential [35]. The functions of the initial $p\,^{13}$N and final ^{14}O states are characterized by specific quantum numbers, including the Young diagrams f, which determine the permutation symmetry of the orbital part of relative motion WFs of these states. Thus, the problem can be reduced to two parts:

i. a construction of $p\,^{13}$N interaction potentials with the FS for each partial wave, i.e., for the given orbital angular momentum L, which also includes a point-like Coulomb term;

ii. the numerical solution of the radial Schrödinger equation for these potentials to find the corresponding WFs of the relative motion.

Furthermore, following Refs. [29,31–33,35], we use well-known expressions for total cross sections and matrix elements of multipole transition operators with the initial and final channel spins $S_i = S_f = S$:

$$\sigma_c(NJ, J_f)$$

$$= \frac{8\pi K e^2}{\hbar^2 k^3} \frac{\mu}{(2S_1 + 1)(2S_2 + 1)} \frac{J + 1}{J[(2J + 1)!!]^2} A_J^2(NJ, K)$$

$$\times \sum_{L_i J_i} P_J^2(NJ, J_f, J_i) I_J^2(J_f, J_i), \qquad (2)$$

where the notation NJ corresponds to EJ for the electric and MJ for the magnetic transitions, respectively. The matrix elements of the EJ transitions have a form

$$P_J^2(EJ, J_f, J_i)$$

$$= (2J + 1)(2L_i + 1)(2J_i + 1)(2J_f + 1)$$

$$\times (L_i 0 J 0 | L_f 0)^2 \begin{Bmatrix} L_i & S & J_i \\ J_f & J & L_f \end{Bmatrix}^2, \qquad (3)$$

and

$$A_J(EJ, K) = K^J \mu^J \left(\frac{Z_1}{m_1^J} + (-1)^J \frac{Z_2}{m_2^J} \right), \qquad (4)$$

$$I_J(J_f, J_i) = \langle \chi_f | r^J | \chi_i \rangle. \qquad (5)$$

In Eqs. (2)–(5), e is the elementary charge, $K = \frac{E_\gamma}{\hbar c}$ is the wave number of the emitted photon with energy E_γ, k is the wave number of particles in the initial channel, m_1, m_2, Z_1, Z_2, and μ are masses and charges of colliding nuclei and their reduced mass, respectively, in the initial channel, S_i, S_f, L_i, L_f, J_i, J_f are the total spins, orbital momenta, total momenta of particles in the initial (i) and final (f) channels, respectively, while $(L_i 0 J 0 | L_f 0)$ are the Clebsch-Gordan coefficients and $\{:::\}$ are the $6j$ symbols. The integral $I_J(J_f, J_i)$ is defined by using WFs of relative motion of particles in the initial $\chi_i(r)$ and final $\chi_f(r)$ states, which depend on an intercluster distance r.

Using the general form for MJ transitions for arbitrary rank J, the matrix element in Eq. (2) can be written by means of the $9j$ symbols as

$$P_J^2(MJ, J_f, J_i) = S(S + 1)(2S + 1)(2J_i + 1)(2L_i + 1)$$

$$\times (2J - 1)(2J + 1)(2J_f + 1)$$

$$\times (L_i 0 J - 1 0 | L_f 0)^2 \begin{Bmatrix} L_i & J - 1 & L_f \\ S & 1 & S \\ J_i & J & J_f \end{Bmatrix}^2, \qquad (6)$$

$$A_J(MJ, K) = \frac{\hbar K}{m_0 c} K^{J-1} \sqrt{J(2J + 1)}$$

$$\times \left[\mu_1 \left(\frac{m_2}{m} \right)^J + (-1)^J \mu_2 \left(\frac{m_1}{m} \right)^J \right], \qquad (7)$$

$$I_J(J_f, J_i) = \langle \chi_f | r^{J-1} | \chi_i \rangle, \qquad (8)$$

where m is a mass of a nucleus in the final channel, μ_1 and μ_2 are magnetic momenta of the clusters, and the remaining notations are the same as in Eqs. (2)–(4).

Thus, to find the cross section of the ^{13}N$(p, \gamma)^{14}$O reaction one should calculate the expressions (5) and (8) for EJ and MJ transitions, respectively. The latter requires finding the radial WFs χ_i and χ_f of the relative motion of particles in the initial and final states.

III. CLASSIFICATION AND STRUCTURE OF STATES

Let us now consider a classification of the $p\,^{13}$N system orbital states according to the Young diagram. It was previously shown that the ground bound state (GS) of ^{13}N and ^{13}C nuclei corresponds to the Young orbital diagram {4441} [36,40]. Recall that possible Young orbital diagrams in the system of $N = n_1 + n_2$ particles can be defined as a direct external product of the orbital diagrams of each subsystem [41,42], which for the $p\,^{13}$N system within the $1p$ shell gives $\{1\} \times \{4441\} \to \{5441\} + \{4442\}$. The first of the obtained diagrams is compatible with orbital momentum $L = 1, 3$ and is forbidden for the s shell, since there cannot be five nucleons in the s shell, while the second diagram is

allowed and compatible with the orbital momenta zero and two [41,42]. Thus, the potential of the $^3S_1$ (here and below we use notations $^{2S+1}L_J$ for resonances) wave has only the allowed state, but the P and F waves have both forbidden and allowed states [27]. However, since we do not have complete tables of the products of Young diagrams for a system with a number of particles greater than eight [43], which we used earlier for such calculations [29,31], the result obtained above should be considered only as a qualitative estimate of possible orbital symmetries in the ground state of ^{14}O nucleus for the $p\,^{13}$N channel.

We now consider the basic characteristics of the ^{14}O nucleus, which has in the GS $J^\pi = 0^+$ the energy 4.628 MeV [27]. Since for the ^{13}N nucleus $J^\pi = 1/2^-$ [27], the GS of ^{14}O in the $p\,^{13}$N channel can be associated with the $^3P_0$ state. Below this threshold, there are no bound excited states (ESs) [27]. Above the threshold, there are the following resonance states (RSs):

1. For the first resonance, which plays the most important role in determining the magnitude of the astrophysical S factor, new data [17] lead to an excitation energy of 5.164(12) MeV (here and below numbers in parentheses are uncertainties), which corresponds to the energy $E_{\text{res}} = 536(12)$ keV relative to the threshold in the center-of-mass (c.m.), the width $\Gamma_{\text{res}} = 38(2)$ keV, and momentum $J^\pi = 1^-$. Previously in Ref. [28] it was reported for this level the excitation energy of 5.156(2) MeV, i.e., $E_{\text{res}} = 0.528(2)$ MeV, and the width $\Gamma_{\text{res}} = 37.3(9)$ keV. In an earlier work [27], for this resonance the excitation energy 5.173(10) MeV, i.e., $E_{\text{res}} = 545(10)$ keV and the width $\Gamma_{\text{res}} = 38.1(1.8)$ keV were reported. In fact, these three results lead to the same 38(2) keV width. However, the resonance energies do not overlap within the experimental errors and can be in the range of $E_{\text{res}} = 524$–555 keV. This resonance can be matched to the $^3S_1$ state, and the $E1$ transition $^3S_1 \rightarrow {}^3P_0$ is possible. It is clear that it cannot be $^3D_1$ because this needs protons in the $1d_{3/2}$ shell (in the framework of a shell-model scheme), which is much higher in energy and likely irrelevant for this state. In this paper, we consider the $E1$ transition $^3S_1 \rightarrow {}^3P_0$.

   All other resonances, as can be seen below, do not make a significant contribution to the S factor at low energies, and their energies, as follows from Refs. [17] and [28], practically overlap. Therefore, we use the data from Ref. [28], but for a comparison we also give the energies and widths obtained in Ref. [17].

2. At an excitation energy of 5.710(20) or 1.082(20) MeV relative to the channel's threshold in the c.m., there is a state $J^\pi = 0^-$ with a width of 400(45) keV [28] which can be associated with a $^1S_0$ wave. However, in this case, the transition to the GS is impossible, because it refers to a triplet state. Let us mention that the classification of allowed transitions is defined by the algebra of the geometric addition of angular momenta, represented by the Clebsch-Gordan coefficients, $6j$ and $9j$ symbols [44,45]. Besides, EJ and MJ transitions change the parity of the initial and final states according

to $(-1)^j$ and $(-1)^{j+1}$, respectively. So, for example, the $^1S_0 \rightarrow {}^2P_0$ transition is not allowed because there is no E or M transition connecting the 0^- and 0^+ states, as is seen from Eqs. (3) and (6).

3. At an excitation energy of 5.920(10) MeV, i.e., $E_{\text{res}} = 1.29(10)$ MeV, there is a state $J^\pi = 1^+$ with a width $\Gamma_{\text{res}} < 12$ keV [17], which can be matched to a $^3P_0$ wave. In Ref. [17] the energy 5.931(10) MeV and the width less than 12 keV were reported. From this wave, magnetic transitions to the GS are impossible.

4. At an excitation energy of 6.284(9) MeV [$E_{\text{res}} = 1.656(9)$ MeV in the c.m.], there is a state $J^\pi = 3^-$ with the width $\Gamma_{\text{res}} = 25(3)$ keV [28], while in Ref. [17] the energy 6.285(12) MeV and the width 37.7(17) keV are obtained. This state can be matched to a $^3D_3$ wave. From this wave, only the $E3$ transition is possible. The $E3$ transition is omitted in our consideration, because of its smallness.

5. At an excitation energy of 6.609(10) MeV [$E_{\text{res}} = 1.981(10)$ MeV], there is a state $J^\pi = 2_1^+$ with a width $\Gamma_{\text{res}} < 5$ keV [28], which can only be associated with a $^3P_2$ or $^3F_2$ waves. In Ref. [17] the energy 6.585(11) MeV and the width less than 25 keV are reported. For $^3F_2$ wave the $E2$ transition is possible and we evaluate its effect.

6. At an excitation energy of 6.767(11) MeV [$E_{\text{res}} = 2.139(11)$ MeV], there is a state $J^\pi = 2^-$ with the width $\Gamma_{\text{res}} < 90(5)$ keV [28]. Based on the results [17], the energy is 6.764(10) MeV and the width is 96(5) keV. This state can be associated with a $^3D_2$ wave. From this wave, only the $M2$ transition to the GS is possible. This transition is omitted, because we restrict ourselves with the consideration of the $M1$ transition only.

7. At an excitation energy of 7.768(10) MeV [3.140(10) MeV in the c.m.] for the state $J^\pi = 2_2^+$ the width of 68(6) keV was observed in Ref. [17], while Ref. [28] reported 7.745(19) MeV [$E_{\text{res}} = 3.117(19)$] and 62(10) keV for the energy and the width, respectively. This resonance state can be associated with the $^3P_2$ or $^3F_2$ waves. From the $^3F_2$ wave the $E2$ transition to the GS is possible and we evaluate its effect.

8. Recently, in Ref. [17] at the excitation energy of 9.755(10) or 5.123(11) MeV relative to the threshold of the $p\,^{13}$N channel, a state $J^\pi = 2_3^+$ with the width $\Gamma_{\text{res}} = 229(51)$ keV was observed. While the excitation energy is in good agreement with the results from Ref. [28], 9.751(11) MeV, the width of the resonance is almost twice as large. Moreover, a momentum $J^\pi = 2_3^+$ of this state was in question in Ref. [28], but in a recent work [17] it was finally determined. This state can also be associated with $^3P_2$ or $^3F_2$ waves. From the $^3F_2$ wave the $E2$ transition to the GS is also possible, and we will consider its effect.

Schematic of energy levels of ^{14}O are shown in Fig. 1. Following Ref. [17] we are using subscripts for the $J^\pi = 2^+$ states. It is worth noticing that the appearance of states with the same momentum J^π, *ad hoc* 2_1^+, 2_2^+, and 2_3^+ in Fig. 1, considered in points 5, 7, 8 above are under detailed discussion

E_x	J_i^π	$\left[^{2S+1}L_J\right] \xrightarrow{NJ} \left[^{2S+1}L_J\right]_f$		
9.751(11)	2_3^+	8. $^3F_2 \xrightarrow{E2} {}^3P_0$		
7.745(19)	2_2^+	7. $^3F_2 \xrightarrow{E2} {}^3P_0$		
6.767(11)	2^-	6. $^3D_2 \xrightarrow{M2} {}^3P_0$	Data on the 1st excited state	
6.609(10)	2_1^+	5. $^3F_2 \xrightarrow{E2} {}^3P_0$		
6.284(9)	3^-	4. $^{2S+1}D_3 \xrightarrow{E3} {}^3P_0$	5.173(10)	1^- 1991, Ajzenberg [28]
5.920(10)	0^+	3. forbidden	5.164(12)	1^- 2019, Charity [17]
5.710(20)	0^-	2. forbidden		
5.156(2)	1^-	1. $^3S_1 \xrightarrow{E1} {}^3P_0$	5.156(2)	1^- 2016, Sukhoruchkin [29]

$$\frac{p\,^{13}\text{N}}{4.628} \qquad\qquad \frac{p\,^{13}\text{N}}{4.628}$$

J_f^π

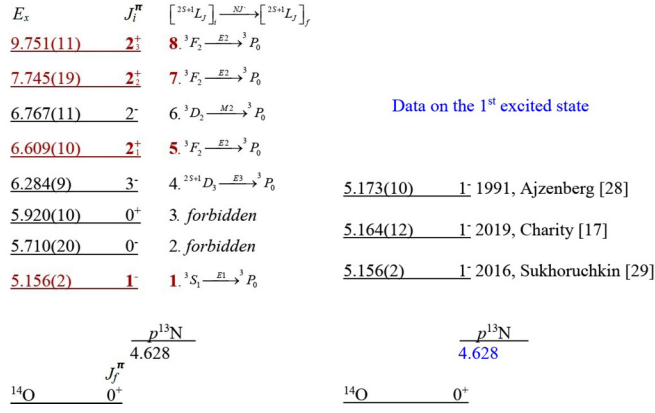^{14}O $\quad 0^+$ $\qquad\qquad$ ^{14}O $\qquad 0^+$

FIG. 1. Schematic of energy levels of ^{14}O (not to scale). The left panel shows the energy levels of ^{14}O according to Ref. [17] and a visual summary of the resonance states analyzed in Sec. III matching the γ-quantum emission of EJ and MJ multiplicity. The energy spectrum illustrates the correspondence to the resonance behavior of phase shifts in the $p\,^{13}$N scattering channel presented in Fig. 2. The right panel shows detailed data on the 1^- excited state. The excitation energies E_x are given in MeV.

in Ref. [17]. To describe spectra of ^{14}O resonances and their properties, the authors used the shell model embedded in the continuum (SMEC) based on the different internal coupling schemes due to the complicated interaction potentials and configuration mixing (see Refs. [1–5,24–26] in Ref. [17] for SMEC applications). While the nature of 2_1^+ and 2_3^+ states is quite transparent, the 2_2^+ state is declared as the partner of the new 0_3^+ state with a width $\Gamma_{\rm res} = 128$ keV lying at 7.669(53) MeV [17].

As a result of the analysis of the above-mentioned resonances, it turns out that, first of all, it is necessary to consider the $E1$ transition from the first resonance at $E_{\rm res} = 536(12)$ keV with $J^\pi = 1^-$ and the width $\Gamma_{\rm res} = 38(2)$ keV [17]. In addition, we consider two other values for the energy of this resonance $E_{\rm res} = 528(2)$ keV with the width $\Gamma_{\rm res} = 37.3(9)$ keV [28] and $E_{\rm res} = 545(10)$ keV with the width $\Gamma_{\rm res} = 38.1(1.8)$ keV [27]. In addition to the $E1$ transition, there are three $E2$ transitions for $J^\pi = 2_1^+$, $E_{\rm res} = 1.981(10)$ MeV, $\Gamma_{\rm res} = 5$ keV, $J^\pi = 2_2^+$, $E_{\rm res} = 3.140(10)$ MeV, $\Gamma_{\rm res} = 68(6)$ keV, and $J^\pi = 2_3^+$, $E_{\rm res} = 5.123(11)$ MeV, $\Gamma_{\rm res} = 229(51)$ keV resonance states, which are admissible and can be associated with the $^3F_2$ wave. We also consider the $M1$ transition for the $J^\pi = 1^+$, $E_{\rm res} = 1.29(10)$ MeV of a non-resonance $^3P_1$ scattering wave to the GS of ^{14}O. Resonances with higher energies either have a large momentum, or their momentum is not determined at all [28] and are not considered here.

IV. INTERACTION POTENTIALS

To find the radial wave functions χ_i and χ_f of the relative motion of particles in the initial and final states, respectively, one should solve the Schrödinger equation with potentials that describe the $p\,^{13}$N scattering process and the states of the residual ^{14}O nucleus. The $p\,^{13}$N potentials for each partial wave, i.e., for the given orbital angular momentum L have a point-like Coulomb term, and a nuclear part of the $p\,^{13}$N interaction. The nuclear part of potential can be written in the one-range Gaussian form as [31,35]

$$V(r, SLJ) = -V_0(SLJ) \exp[-\alpha(SLJ)r^2], \qquad (9)$$

where r is the distance between the proton and ^{13}N, $V_0(SLJ)$ is the depth of the potential, and $\alpha(SLJ)$ is the range parameter for a given S, L, and J, respectively. Resonance potentials were constructed in such a way as to correctly describe the energy and width of such resonances.

The interaction (9) is given as a two-parameter Gaussian potential, i.e., with just an LSJ-dependent central term, and the consideration of Pauli-forbidden states is based on Young diagrams. Each state is described independently, so the potential for each partial wave effectively includes all features such as spin-orbit and spin-spin terms, but without separation in operator terms. There are different approaches and prescriptions related to the choice of the potential parametrization. In this study we are using the one-range Gaussian potential (9), which has only two fitting parameters, due to its simpler form than the Woods-Saxon and also because at studies of the radiative capture processes at low energies this potential allows complete description of all basic characteristics of the process. Over 30 radiative capture reactions have been successfully described (see Refs. [31,35] and citations therein) using the one-range Gaussian potential. One can also mention that a comparison of studies of a radiative capture process using the Woods-Saxon potential [46] and a simple one-range Gaussian potential [47] shows that the latter potential provided a good description of the process. Besides, the use of the Gaussian potential is easy due to the fact that the expansion of the WF in terms of the Gaussian basis within the variation method [31] the majority of matrix elements are obtained in a closed analytical form.

In calculations, we use for the proton mass $m_p = 1.007\,276\,469$ atomic mass units (amu) [48] and ^{13}N mass $13.005\,736\,7$ amu [49], where 1 amu $= 931.494\,102\,4$ MeV [48] and the constant $\hbar^2/m_0 = 41.4686$ MeV fm^2. The Coulomb potential at $R_C = 0$ is written in MeV as $V_C(r) = 1.439\,975Z_1Z_2/r$, where r is the interparticle distance in fm, Z_1 and Z_2 are charges of the particles in units of the elementary charge. The Sommerfeld parameter $\eta = \mu Z_1 Z_2 e^2 / (k\hbar^2) = 3.44476 \times 10^{-2} \mu Z_1 Z_2 / k$, where $k = (2\mu E/\hbar^2)^{1/2}$ is the wave number specified in fm^{-1} and defined by the energy E of interacting particles and the reduced mass μ of these particles in amu.

Following Ref. [50] for calculations of the width and employing the resonance-scattering phase, we use the expression $\Gamma_{\rm res} = 2(d\delta/dE)^{-1}$, where δ is the phase shift. For descriptions of the $^3S_1$, $^3P_1$, and $^3F_2$ scattering states we use the corresponding experimental energies and widths. For the $^3S_1$ resonance, three different experimental measurements are reported for the resonance energy and width. Therefore, we constructed the potential for the $^3S_1$ resonance-scattering phase with three sets of parameters. In Table I are given the results of calculations of parameters for the corresponding potential. The potential with sets of parameters 1a, 1b, and 1c reproduce the resonance energies 528, 536, and 545 keV,

TABLE I. List of transitions from the initial $\{^{(2S+1)}L_J\}_i$ state to $^3P_0$ GS of the ^{14}O nucleus. The value of P^2 determines the coefficient in expressions (3) and (6). The width $\Gamma_{\rm res}$ and $S(0)$ factor are obtained by using the potential parameters V_0 and α. The value $\widetilde{S}(0)$ of the S factor and the set of parameters $1d$, $1e$, and $1f$ for the potential are used for calculations of the resonance width $\widetilde{\Gamma}_{\rm res}$.

Set	$\{^{(2S+1)}L_f\}_i$	Transition	P^2		V_0, MeV	α, fm^{-2}	$E_{\rm res}$, MeV	$\Gamma_{\rm res}$, keV	$S(0)$, keV b	$\widetilde{\Gamma}_{\rm res}$, keV	$\widetilde{S}(0)$, keV b
				a	14.955	0.085	0.528(1)	37(1)	8.4(2)		
				b	15.882	0.092	0.536(1)	38(1)	7.9(2)		
1	$^3S_1$ resonance at	$E1$	1	c	18.244	0.11	0.545(1)	37(1)	7.0(2)		
	0.528, 0.536, 0.545 MeV			d	35.053	0.25	0.528(1)			22(1)	4.8(1)
				e	29.316	0.02	0.536(1)			25(1)	5.1(1)
				f	31.582	0.22	0.545(1)			26(1)	4.9(1)
2	$^3P_1$ no resonance	$M1$	2		555.0	1.0			0.014(1)		
3	$^3F_2$ resonance at 1.981(10)	$E2$	3		698.134	0.36	2.000	13	<0.01		
4	$^3F_2$ resonance at 3.117(19)	$E2$	3		343.613	0.18	3.120	58	<0.01		
5	$^3F_2$ resonance at 5.123(11)	$E2$	3		430.2	0.23	5.127	232	<0.01		

respectively. The latter allows us to find the optimal astrophysical S factor. Figure 2 presents the dependence of the elastic $p^{13}N$ scattering phase shifts on the energy $E_{\rm c.m.}$. The result of the calculation of the $^3S_1$ phase shift with the set $1c$ parameters for the S scattering potential without FS leads to $90° \pm 1°$ at the energy $E_{\rm res} = 0.545$ MeV [27] are presented by the red solid curve. The calculations of the $^3S_1$ phase using the sets of parameters $1a$ and $1b$, which correspond to the resonances at $E_{\rm res} = 0.528$ MeV [28] and $E_{\rm res} = 0.536$ MeV [17], give the coincide results in Fig. 2. Thus, the scattering potentials with the set of parameters $1a$, $1b$, and $1c$ are phase-shift-equivalent potentials.

The potential of the nonresonance scattering is also constructed quite unambiguously based on the scattering phase shifts for a given number of bound states allowed and for-
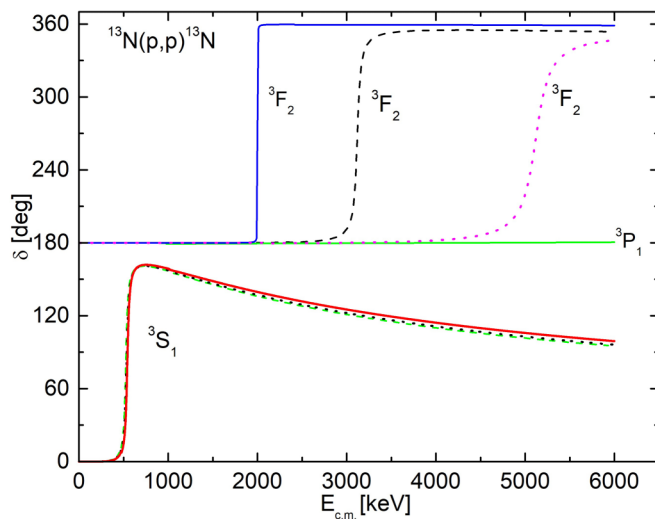

FIG. 2. The dependence of the elastic $p^{13}N$ scattering phases on the energy. Calculations are performed by using the potentials with parameters from Table I. The $^3S_1$ phase shift is calculated by using the set $1a$ (green dashed curve), $1b$ (black dotted curve), and $1c$ (red solid curve) from Table I, respectively. The three sets of parameters for the potential given almost the same results for the $^3S_1$ phase shift. In the given energy region, the $^3P_1$ phase shift has very weak energy dependence.

bidden in the partial wave. The accuracy of determining the parameters of such a potential is primarily associated with the accuracy of extracting the scattering phase shifts from the experimental data. Since the classification of states according to Young diagrams makes it possible to unambiguously fix the bound state number, which completely determines its depth, the potential width at a given depth is determined by the shape of the scattering phase shift. When constructing a nonresonance scattering potential from the data on the spectra of the nucleus, it is difficult to evaluate the accuracy of finding its parameters even for a given number of bound states. Such a potential, as is usually assumed for the energy range up to 1–3 MeV, should lead to the scattering phase shift close to zero or give a smoothly decreasing phase shift shape, since there are no resonance levels in the spectra of the nucleus.

For the $^3P_1$ scattering potential, one can use the parameter set 2 from Table I. Such a potential has the FS and leads to a scattering phase shift of $180° \pm 1°$, which has a very weak dependence on energy and is presented by the green solid curve in the energy range from zero to 7 MeV. Since it has the FS, according to the generalized Levinson theorem, its phase shift begins at $180°$ [37].

We also considered the $J^\pi = 2_1^+$, $E_{\rm res} = 1.981(10)$ MeV, $\Gamma_{\rm res} = 5$ keV, $J^\pi = 2_2^+$, $E_{\rm res} = 3.140(10)$ MeV, $\Gamma_{\rm res} = 68(6)$ keV, and $J^\pi = 2_3^+$, $E_{\rm res} = 5.123(11)$ MeV, $\Gamma_{\rm res} = 229(51)$ keV resonances, which lead to a noticeable change in the S factor in resonance regions, using the potentials with the parameters sets 3, 4, and 5, respectively, from Table I. However, it was not possible to construct such potentials in P waves, therefore, F scattering waves were used here. The first of them leads to a resonance at 2.00 MeV with a width $\Gamma_{\rm res} = 13$ keV shown by the blue solid curve in Fig. 2, the second gives the resonance at $E_{\rm res} = 3.12$ MeV and a width $\Gamma_{\rm res} = 58$ keV and is presented by the black dashed curve, while the phase shift of the third resonance at $E_{\rm res} = 5.127$ MeV is shown by the dotted curve. We were not able to obtain the resonance at $E_{\rm res} = 1.981$ MeV with the width $\Gamma_{\rm res} < 5$ keV, as given in Ref. [28], but the obtained value is completely consistent with the recent data [17].

To build the potential for the description of the GS of ^{14}O, we use the experimental binding energy and the asymptotic normalization coefficient (ANC) A_{NC} of this state. The

corresponding potentials are tested based on the calculation of the root mean square charge radius of ^{14}O.

In Ref. [15] the value of $A_{NC} = 5.42(48)$ fm$^{-1/2}$ and the proton spectroscopic factor $S_p = 1.88(34)$ are given. A similar value of $A_{NC} = 5.42(74)$ fm$^{-1/2}$ is also reported in Ref. [16], while Ref. [22] reports $A_{NC} = 5.39(38)$ fm$^{-1/2}$. Using the results of Ref. [15] for the ANC and the expression for the asymptotic normalization constant

$$A_{NC} = \sqrt{S_p} C, \qquad (10)$$

one gets $C = 4.04(72)$ fm$^{-1/2}$. For the determination of C, the following definition is also used (see, for example, Ref. [51]):

$$\chi_L(r) = C W_{-\eta, L+1/2}(2k_0 r), \qquad (11)$$

where $W_{-\eta, L+1/2}(2k_0 r)$ is a Whittaker function. We use a different definition of ANC [52]

$$\chi_L(r) = \sqrt{2k_0} C_w W_{-\eta, L+1/2}(2k_0 r), \qquad (12)$$

which differs from the previous definition by the factor $\sqrt{2k_0}$ which in this case is 0.956. Then, for the dimensionless C_w, we get $C_w = 4.23(75)$. At the same time in Ref. [22] $S_p = 0.90(23)$ was given for the spectroscopic factor, which yields $A_{NC} = 5.39(38)$ fm$^{-1/2}$ and allows us to obtain $C_w = 6.15(1.22)$. $A_{NC} = 30.4(7.1)$ fm^{-1} and $S_p = 1.94(45)$ were obtained in Ref. [23], which lead to the dimensionless asymptotic normalization constant within the range 3.26–5.30 with an average of 4.28(1.02).

The potential of a bound ground $^3P_0$ state with the FS should correctly reproduce the GS energy 4.628 MeV of the ^{14}O nucleus with $J^\pi = 0^+$ in the $p\,^{13}$N channel [27], and it is reasonable to describe the mean square radius of ^{14}O as well. Since data on the radius of ^{14}O are not available, we consider it to coincide with the radius of ^{14}N, the experimental value of which is 2.5582(70) fm [49]. As a result, we obtained the following parameters for the GS potential, which lead to $C_w = 4.1(1)$:

$$V_0(1, 1, 0^+) = 226.230 \text{ MeV}, \quad \alpha(1, 1, 0^+) = 0.23 \text{ fm}^{-2}. \qquad (13)$$

The potential (9) with the parameters (13) gives for the ^{14}O nucleus the binding energy of 4.628 MeV and the root mean square charge radius $R_{ch} = 2.55$ fm. We used 0.8768(69) fm for the proton radius [48] and 2.4614(34) fm for the ^{13}N radius. The latter radius was taken to be the radius of ^{13}C [49], because the ^{13}N radius is not available.

The GS potential which leads to $C_w = 6.1(1)$ has the parameters

$$V_0(1, 1, 0^+) = 156.728 \text{ MeV}, \quad \alpha(1, 1, 0^+) = 0.15 \text{ fm}^{-2}. \qquad (14)$$

The GS potential with parameters (14) gives a binding energy of 4.628 MeV and the root mean square charge radius $R_{ch} = 2.63$ fm. One can see that the potential (14) gives a larger radius than the potential (13), so by simple estimates it is clear the GS with (14) should have larger cross sections.

We calculated the radial WFs of GSs and shape of the integrand in matrix element ME (5) of the $E1$ transition using the scattering potential with the set of parameters 1a and 1c from Table I. The results of calculations are presented in Fig. 3. The

radial WFs for the GS of ^{14}O in the $p\,^{13}$N channel obtained with potentials (13) and (14) are shown in Fig. 3(a). The GS WFs have the same behavior, different magnitudes, and the shifted nodes. The different magnitudes lead to the different shape of the integrand in the ME (5) of the $E1$ transition, which also depends on the choice of the parameters for the potential for the description of the scattering state. The node in the nuclear interior leading to the node in the integrand shown in Fig. 3(b) and 3(c), respectively. We should note that integrands in the ME (5) of the $E1$ transition almost coincide with the integrand shown in Fig. 8 in Ref. [22].

One should note that the shell model is undoubtedly the most perfectly formulated from both a physical and mathematical point of view. In fact, on the one hand, in the framework of the shell model, the Pauli principle is precisely taken into account. On the other hand, this model allows, based on algebraic methods, to take into account the effects of clustering in atomic nuclei. Thus, the shell model could be recognized as a criterion for testing the "quality" of other models by using phenomenological nucleon-cluster potentials. Let us for comparison consider the GS potentials without FS and scattering potentials with the FS in the $^3S_1$ wave based on a single-particle model. The GS potential without the FS has parameters

$$V_0(1, 1, 0^+) = 61.23803 \text{ MeV}, \quad \alpha(1, 1, 0^+) = 0.13 \text{ fm}^{-2}. \qquad (15)$$

This potential leads to the binding energy of 4.628 00 MeV, root mean square charge radius $R_{ch} = 2.54$ fm, and $C_w = 4.1(1)$. This completely coincides with the option for potential (13). One can also obtain another option for the GS potential, which agrees with the shell model of the system, which has parameters

$$V_0(1, 1, 0^+) = 45.46913 \text{ MeV}, \quad \alpha(1, 1, 0^+) = 0.085 \text{ fm}^{-2}. \qquad (16)$$

This potential leads to the binding energy of 4.62800 MeV, root mean square charge radius $R_{ch} = 2.61$ fm, and $C_w = 6.0(1)$. This coincides with the option for potential (14). The scattering potential for the resonance $^3S_1$ wave now has the FS and parameters

$$V_0(1, 1, 0^+) = 125.529 \text{ MeV}, \quad \alpha(1, 1, 0^+) = 0.24 \text{ fm}^{-2}. \qquad (17)$$

This potential leads to the resonance energy of 545 keV and its width of 37(1) keV, which completely coincides with results for the set 1c from Table I. The shape of the integrands in ME (5) of the $E1$ transition for the GS potentials (15) and (16) and scattering potential (17) is shown in Fig. 3(d).

We use the potentials with parameters from sets 1a, 1b, and 1c in Table I for the description of the resonance states and parameters (13) and (14) for the description of the residual ^{14}O nucleus for calculations of the ^{13}N$(p, \gamma)^{14}$O reaction rate and the astrophysical S factor.

The astrophysical S factor was calculated previously by using the $^3S_1$ resonance scattering. Using the values of $\widetilde{S}(0)$ from Table I, we consider the inverse problem to construct potentials for a description the $^3S_1$ resonance based on the resonance energies and the corresponding astrophysical S factor.
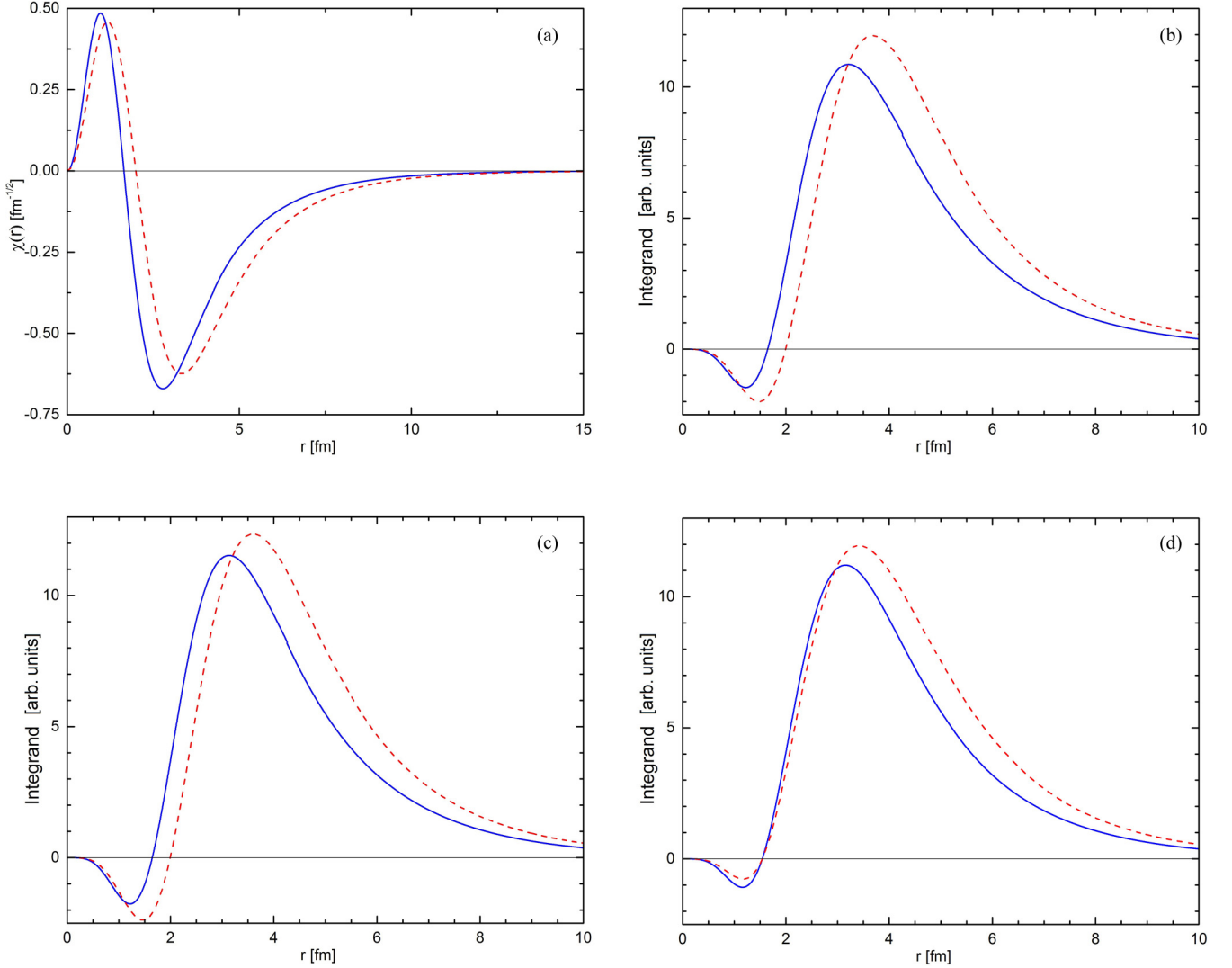
FIG. 3. The radial part of the GS wave functions ^{14}O in the $p\,^{13}$N channel and integrands in the matrix element (5) for the $E1$ transition in arbitrary units (arb. units). (a) The GS wave function obtained with potential (13) (solid curve) and potential (14) (dashed curve). (b) The integrand of the $E1$ transition ME (5) for the scattering potential with the set of parameters $1a$ from Table I and for the GS potential (13) (solid curve) and (14) (dashed curve), respectively. (c) The integrand of the $E1$ transition ME (5) for the scattering potential with the set of parameters $1c$ from Table I and for the GS potential (13) (solid curve) and (14) (dashed curve), respectively. (d) The integrand of the $E1$ transition ME (5) for the GS potential without FS (15) at $C_W = 4.1$ (solid curve) and the GS potential without FS (16) at $C_W = 6.0$ (dashed curve) and for the scattering potential (17), respectively.

The parameters of these potentials are given in Table I as sets $1d$, $1e$, and $1f$.

V. REACTION RATE AND ASTROPHYSICAL S FACTOR OF THE PROTON RADIATIVE CAPTURE ON ^{13}N

Let us calculate the reaction rate for the ^{13}N$(p, \gamma)^{14}$O radiative capture and the astrophysical S factor using the total cross section (2) and corresponding matrix elements of multipole transition operators. The astrophysical factor $S(E)$ is defined as

$$S(E) = E\sigma_c(NJ, J_f)e^{-2\pi\eta}, \tag{18}$$

where the factor $\exp(-2\pi\eta)$ approximates the Coulomb barrier between two point-like particles with charges Z_1 and Z_2 and orbital momentum $L = 0$, while the reaction rate is commonly expressed in cm^3 mol^{-1} s^{-1} and is determined according to Ref. [25,53] as

$$
\begin{aligned}
N_A\langle\sigma_c v\rangle &= N_A \frac{2(2/\pi)^{1/2}}{\mu^{1/2}(k_B T)^{3/2}} \int_0^\infty \sigma_c(E)E \exp(-E/k_b T)dE \\
&= 3.7313 \times 10^4 \mu^{-1/2} T_9^{-3/2} \\
&\quad \times \int_0^\infty \sigma_c(E)E \exp(-11.605E/T_9)dE. \tag{19}
\end{aligned}
$$

In Eq. (19), N_A is Avogadro's number, k_B is Boltzmann's constant, E is the energy in the center-of-mass frame given in MeV, the cross section $\sigma_c(E)$ is measured in μb, μ is the reduced mass in a.m.u., and T_9 is the temperature in units
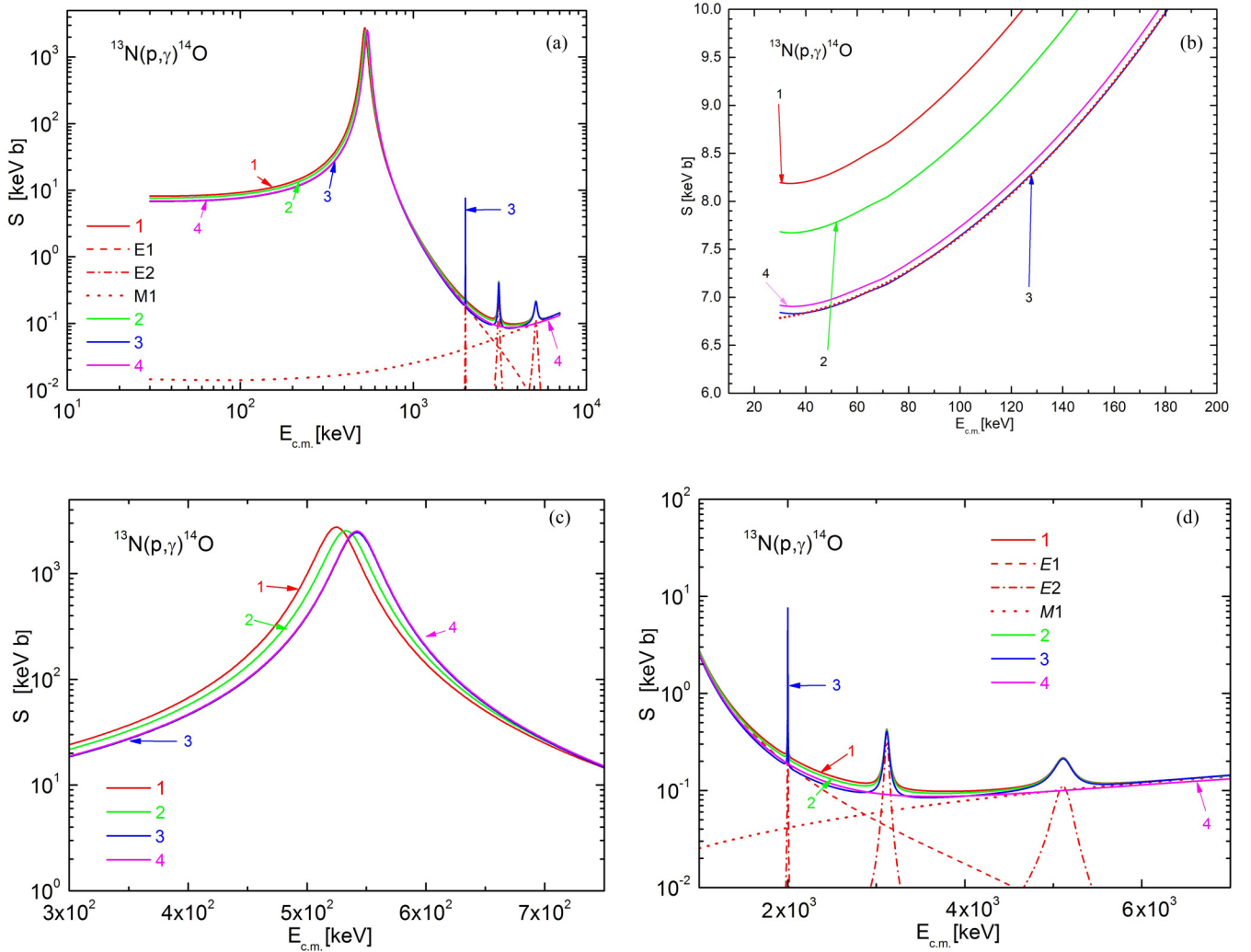
FIG. 4. Astrophysical S factor of the proton radiative capture on ^{13}N. (a) The energy range is 30 keV to 7 MeV. The solid curves 1–4 present results of calculations which include the sum of $E1$, $E2$, and $M1$ transitions. Results presented by curves 1–3 are obtained by using potential with the set of parameters $1a$, $1b$, and $1c$ from Table I, respectively, and the GS potential (13). The curve 4 corresponds to the "node inversion" in the $E1$ transition simulated by the GS potential without FS (15) and scattering potential (17). The dashed, dash-dotted, and dotted curves illustrate the contributions of the $E1$, $E2$, and $M1$ transitions, respectively, into S factors obtained for the potentials with the set of parameters $1a$ from Table I and GS (13). (b) The energy range 30–200 keV. The solid curves 1, 2, 3, and 4 present the same results as in panel (a). The red dotted curve, which coincides with curve 3, presents the quadratic approximation (20) of the S factor at low energies. (c) The energy range is 30 keV to 0.7 MeV. Notations are the same as in panel (b). (d) The energy range is 1–7 MeV. Notations are the same as in panel (a).

of 10^9 K. The behavior of the S factor, when resonances are present, in general is expected to be rather smooth at low energies and can be expanded in a Taylor series around $E = 0$ [54,55] as

$$S(E) = S_0 + ES_1 + E^2 S_2. \qquad (20)$$

Essentially, the experimental data are absent on the astrophysical S factor of the proton radiative capture on ^{13}N, but in the database of Ref. [56] there are rates of this reaction from Refs. [7,15]. However, it is clear that the shape of the S factor should mainly be determined by resonance in the $^3S_1$ scattering wave at 0.528 MeV with a width $\Gamma_{res} = 37.3(9)$ keV and $J^\pi = 1^-$ [28]. The contributions of cross sections of $^3F_2$ reso-

nances from Table I, which are determined by $E2$ transitions, are possible as well.

For calculations of the astrophysical S factor we use the potentials with parameters from sets $1a$, $1b$, and $1c$ in Table I for the description of the resonance state and parameters (13) and (14) for the description of the residual ^{14}O nucleus. We also calculate the width of the $^3S_1$ resonance using the set of parameters $1d$, $1e$, and $1f$ for the potentials from Table I, which were obtained based on the values of the astrophysical S factor.

The results of the calculation of the S factor of the proton radiative capture on ^{13}N to the GS of ^{14}O nucleus include the sum of $E1$, $E2$, and $M1$ transitions are shown in Fig. 4. For the contribution of the $^3S_1$ scattering wave the set of

TABLE II. Astrophysical S factors at zero energy.

Ref.	[26]	[15,16,21–23][a]	[19][b]	[27][a]
S, keV b	3.8^{+1}_{-08}	5–6	2.6	2–2.3

[a]Values are taken from figures in Refs. [16] (Fig. 7), Ref. [17] (Fig. 8), Ref. [18] (Fig. 9), Ref. [23] (Fig. 5), Ref. [25] (Fig. 3), Ref.[27] [Fig. 2(b)].
[b]Value is taken from the approximation at low energies.

parameters from Table I for the potential and potential (13) for the GS are considered. We calculated the contributions of the $M1$ transition $^3P_1 \rightarrow {}^3P_0$, as well as the resonance $E2$ transitions into the S factor by using the set of potentials 2, 3, 4, and 5 from Table I, respectively, and for the description of the GS the potential (13) was used. The results of these calculations are shown in Fig. 4(a). Analysis of results presented in Fig. 4(a) shows that contributions of the $M1$ and $E2$ transitions in the S factor are negligible at energies $E < 1$ MeV, but are significant at high energies. At the resonance energy, the S factor reaches 2.4 MeV b, which is in good agreement with the results of other works (see, for example, Refs. [7,15,21,22]), where the values for the S factor from about 2.0 to 2.5 keV b were reported. The S factor shown in Fig. 4(b) is given for three sets of parameters 1a, 1b, and 1c, highlighting the differences. Results of our calculations for the S factor for the potentials 1a from Tables 1 and Eq. (13) in the energy range of 30–50 keV lie in the range of 8.2–8.3 keV b, while in the energy range of 30–70 keV, the average value is 8.4(2) keV b. The error given here is determined by averaging the S factor over the above energy range. Known results for the S factor at zero energy lead to a value in the range from 2.0 to 6.0 keV b [7,15,21,22]. We use the GS potential (14) and calculate the S factor in the energy range 30–70 keV by using the set of parameters 1a from Table I for the potential and obtain almost a constant value $S = 11.9(2)$ keV b. At the resonance energy, the S factor reaches 2.9 MeV b, which is noticeably more than the results of Refs. [7,15,21,22]. Therefore, we should mention that the GS potential with the parameters (13) for description of the GS of ^{14}O nucleus in the $p\,^{13}$N channel at the low-energy region leads to more preferable results for the astrophysical S factor, which are quite consistent with results from previous calculations. Our calculations for the S factor with the parameters (14) for the potential of the GS gives too high of a value for the S factor at low energies. However, since there are no experimental measurements of the S factor for this reaction, no final conclusions can be drawn.

Table II displays the compilation of the results for the astrophysical S factors at zero energy obtained in different works. As can be seen from Table II, the deviation of data for the S factor is in the range from 2 to 6 keV b, although the most recent value is apparently given in Ref. [26]. We use the sets of parameters 1a, 1b, and 1c for the potential of $^3S_1$ scattering from Table I and potential (13) for the GS, which reproduce accurately the position and width of resonances, and calculate the corresponding S factors. The results are presented in Table I. Depending on the resonance energy, the S factors are 8.4(2) keV b [$E_{\text{res}} = 528(1)$ keV], 7.9(2) keV b [$E_{\text{res}} = 536(1)$ keV], and 7.0 keV b [$E_{\text{res}} = 545(1)$ keV]. The

potential with the set 1a from Table I accurately reproduces the width average value of 37 keV [28] and leads to $S(0) = 8.4(2)$ keV b. The potential with the set 1b reproduces the resonance energy of 536(12) keV and the width $\Gamma_{\text{res}} = 38(2)$ keV from Ref. [17]. The corresponding average value for the S factor at 30–70 keV is $S(0) = 7.9(2)$ keV b, which is slightly less than for the S scattering potential 1a. We consider a potential with parameters 1c, which leads to the resonance at 545 keV and a width $\Gamma_{\text{res}} = 37(1)$ keV [27]. This potential gives $S(0) = 7.0(2)$ keV b.

Nevertheless, let us try to find out whether it is possible within our approach to obtain the S factor at zero energy that is close to the results of Ref. [26], namely, 3.8^{+1}_{-08} keV b. We constructed S wave scattering potentials, which with the potential (13) for the GS allow us to obtain maximum value of the S factor at about 4.8–5.0 keV b given in Ref. [26]. Such potentials have the set of parameters 1d, 1e, and 1f listed in Table I. These potentials lead to the resonance energies 528(1), 536(1), and 545(1) keV, respectively, but the corresponding widths are significantly smaller than reported in Refs. [17,27,28]. In particular, the set 1d leads to $E_{\text{res}} = 528(1)$ keV, but the width is $\widetilde{\Gamma}_{\text{res}} = 22(1)$ keV. At 30 keV, $\widetilde{S}(0) = 4.8$ keV b and its average value in the range of 30–70 keV is $\widetilde{S}(0) = 4.8(1)$ keV b. If for the potential with a resonance energy of 536 keV, we use the parameters 1e from Table I, which lead to $\widetilde{\Gamma}_{\text{res}} = 25(1)$ keV, then the S factor decreases to $\widetilde{S}(0) = 5.1(1)$ keV b. The S factor decreases to $\widetilde{S}(0) = 4.9(1)$ keV b when we use the set 1f for the potential and the width becomes $\widetilde{\Gamma}_{\text{res}} = 26(1)$ keV. Thus, in principle, all previously obtained results for the S factor at zero energy can be reproduced, but the width of the resonances does not correspond to the data [17,27,28]. Therefore, for the considered resonance energies, if we correctly describe their widths, it is impossible to obtain the S factor below 7.0(2) keV b. Only a decrease in the resonance width to 25–26 keV with its energy of 536–545 keV leads to an S factor of the order of 4.9–5.1 keV b.

We also calculated the S factor using the GS potential (15) without FS and the scattering potential (17). The result for the average value of the S factor in the range of 30–70 keV is 7.0(1) keV b that completely coincides with the S factor, calculated with the parameters set 1c from Table I and GS potential (13). We use Eq. (20) for the approximation of the S factor at low energies. The corresponding parameters are $S_0 = 6.7645$, $S_1 = -2.7612 \times 10^{-3}$, $S_2 = 1.1428 \times 10^{-4}$ at $\chi^2 = 1.0 \times 10^{-3}$. The results are shown in Fig. 4(b) by the dotted curve that coincides with the curve 3, which presents the results of calculations for the potentials with the set of parameters 1c from Table I and GS (13).

Using Eq. (19), we calculated the rate of the ^{13}N$(p, \gamma)\,^{14}$O radiative capture by considering the sum of $E1$, $M1$, and $E2$ transitions. The dependence of the ^{13}N$(p, \gamma)\,^{14}$O reaction rate on astrophysical temperature is shown in Fig. 5. The corresponding rates are tabulated in Table III for $0.01 < T_9 < 10$. The calculations are performed by using the set of parameters 1c and (13) for the potentials. Let us mention that the earlier calculations [15,21,22] practically coincide with our results with small deviations, while results from Ref. [7] at temperatures $T_9 > 1$ are up to two times lower than the present
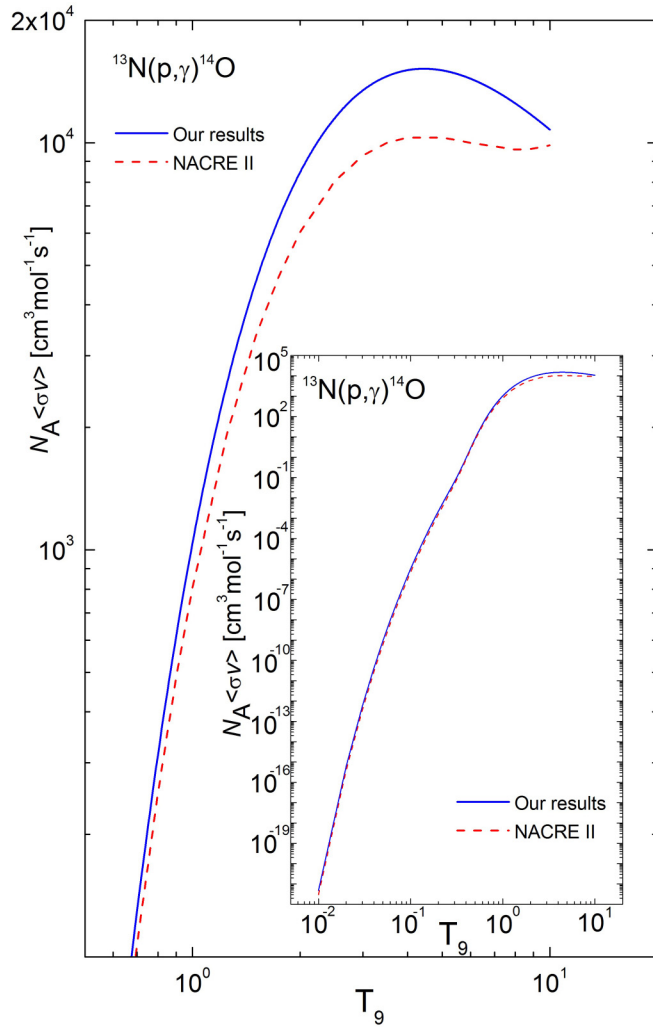
FIG. 5. The dependence of the reaction rate of the ^{13}N$(p, \gamma)^{14}$O radiative capture on astrophysical temperature. The solid curve presents our calculations for the sum of $E1$, $M1$, and $E2$ transitions performed for the potentials with the set of parameters $1c$ from Table I and GS (13), and the NACRE II data [26] are shown by dashed curve. The inset shows the dependence of the reaction rate of the proton radiative capture on ^{13}N on astrophysical temperature in the range of $0.01T_9$–$10T_9$.

results. The results of calculations with the set of parameters $1c$ and (14) for the potentials give a noticeable excess of the reaction rate over the rates obtained with the GS potential (13) at temperatures above $1T_9$.

Following Ref. [57] the reaction rate obtained in our calculations is parametrized as

$$
N_A \langle \sigma v \rangle = \frac{a_1}{T} \exp\left(-\frac{a_2}{T}\right)(1 + a_3 T^{1/3} + a_4 T^{2/3}
$$
$$
+ a_5 T^{4/3} + a_7 T^{5/3} + a_8 T^{6/3} + a_9 T^{7/3})
$$
$$
+ \frac{a_{10}}{T^{1/2}} \exp\left(-\frac{a_{11}}{T^{1/2}}\right) + \frac{a_{12}}{T} \exp\left(-\frac{a_{13}}{T^{1/3}}\right)
$$
$$
+ \frac{a_{14}}{T^{1/3}} \exp\left(-\frac{a_{15}}{T^{1/2}}\right) + \frac{a_{16}}{T^2} \exp\left(-\frac{a_{17}}{T^2}\right). \quad (21)
$$

TABLE III. The results of the dependence of the $p^{13}N$ reaction rate on temperature.

Temperature (T_9)	Reaction rate (cm^3 mol^{-1} s^{-1})
0.01	4.81×10^{-22}
0.02	6.46×10^{-16}
0.03	5.94×10^{-13}
0.04	4.37×10^{-11}
0.05	9.28×10^{-10}
0.06	9.54×10^{-9}
0.07	6.14×10^{-8}
0.08	2.86×10^{-7}
0.09	1.05×10^{-6}
0.1	3.22×10^{-6}
0.11	8.61×10^{-6}
0.12	2.06×10^{-5}
0.13	4.49×10^{-5}
0.14	9.09×10^{-5}
0.15	1.73×10^{-4}
0.16	3.12×10^{-4}
0.17	5.37×10^{-4}
0.18	8.90×10^{-4}
0.19	1.42×10^{-3}
0.2	2.21×10^{-3}
0.25	1.42×10^{-2}
0.3	6.46×10^{-2}
0.35	2.53×10^{-1}
0.4	9.10×10^{-1}
0.45	2.91
0.5	8.04
0.6	4.02×10^1
0.7	1.30×10^2
0.8	3.13×10^2
0.9	6.13×10^2
1	1.04×10^3
1.5	4.53×10^3
2	8.46×10^3
2.5	1.15×10^4
3	1.35×10^4
3.5	1.46×10^4
4	1.51×10^4
4.5	1.52×10^4
5	1.51×10^4
6	1.44×10^4
7	1.35×10^4
8	1.25×10^4
9	1.16×10^4
10	1.08×10^4

The parameters for the reaction rate (21) from Table IV lead to $\chi^2 = 0.006$ and allow us to merge with the calculated reaction rate using Eq. (21). Results of calculations using Eq. (21) are presented in Fig. 5. It almost merges with a blue solid curve that shows the calculated reaction rate using Eq. (19) that is given in Table III. We parametrized the NACRE II data [26] using the same Eq. (21) with $\chi^2 = 0.05$ and 5% errors, which leads to the parameters listed in Table IV. The corresponding results of calculations are shown in Fig. 5 by the dashed curve.

TABLE IV. Parameters of the analytical parametrization of the $^{13}N(p, \gamma)^{14}O$ reaction rate for the present calculations based on Eq. (21) and the NACRE II data [26] based on Eq. (21) as well.

Parameters	a_1	a_2	a_3	a_4	a_5	a_6	a_7
Present work, Eq. (21)	4.68425	5.5271	72207.8	−2.86832	−17716.6	−1304.726	−1155.274
NACRE II	77.14845	4.87776	−2791.957	7554.465	−4686.978	3691.79	−4033.686

Parameters	a_8	a_9	a_{10}	a_{11}	a_{12}	a_{13}	a_{14}
Present work, Eq. (21)	−1020.536	215.4007	4.66187×10^6	10.92388	8.5529×10^7	15.50687	16674.76
NACRE II	1901.048	−309.4704	−3320.309	7.12181	3.13709×10^8	15.87507	−13.31191

Parameters			a_{15}	a_{16}	a_{17}		
Present work, Eq. (21)			7.86955	−77.74082	1.38331		
NACRE II			5.65906	−48.07274	1.23332		

For the detailed comparison of the dependence of the reaction rate on astrophysical temperature, we calculated the ratio of our reaction rate to the rates from Refs. [15,21–23,26]. The results of this comparison are shown in Fig. 6(a). It can be seen from Fig. 6(a) that the results of present calculations exceed NACRE II up to 1.7 times at the lowest temperatures and are almost equal to them at a temperature of $10T_9$. The results of other studies lead to values that go below present calculations up to 1.2 times at a temperature of $0.01T_9$, and in the range of $0.4T_9$–$0.5T_9$ practically coincide with our data. But as the temperature tends to $1T_9$, the values again become less than ours by a factor of 1.2. In Fig. 6(b) are presented the ratios of the reaction rates obtained in the present work and in Refs. [15,21–23] to NACRE II [26] which is parametrized with the parameters from Table IV.

Let us make a comparative analysis for the S factor obtained within our approach and calculated in the R-matrix approach [22,58]. Reference [22] presents the most detailed and accurate uncertainties analysis for the astrophysical S factor, where the uncertainties were investigated by varying five parameters: the ANC for ^{14}O, Γ_γ, Γ_{tot}, and $E_{c.m.}$

of the first resonance. The authors concluded that, with increasing energy, the fractional uncertainty in the S factor drops from 0.31 to 0.21 and the uncertainty of the Γ_γ and the total width of the first resonance Γ_{tot} as well as the ANC make significant contributions to the uncertainty for $E_{c.m.} < 0.6$ MeV [22].

In our model we operate with three experimental input parameters, i.e., ANC, Γ_{tot}, and $E_{c.m.}$. So, the initial score is $5 : 3$. The uncertainty of $E_{c.m.}$ only produces less than 2% [22]. Therefore, it is reasonable to exclude $E_{c.m.}$ among both parameter sets as the consensus holds. Thus, the score drops to $4 : 2$. Γ_γ raises the highest uncertainty to 20%–30% [22].

In our model there is no such uncertainty because we do not subdivide the capture cross section into direct and resonant parts and we operate with ANC and Γ_{tot} only. The signature of the resonances is seen in the phase-shift energy dependence shown in Fig. 2. In our calculations, the resonances are incorporated in natural continuous form without any subdivisions so that there is no need for the Γ_γ parameter. Also, it is important to mention that we are implementing the calculations of the overlap integrals starting from $r = 0$, contrary
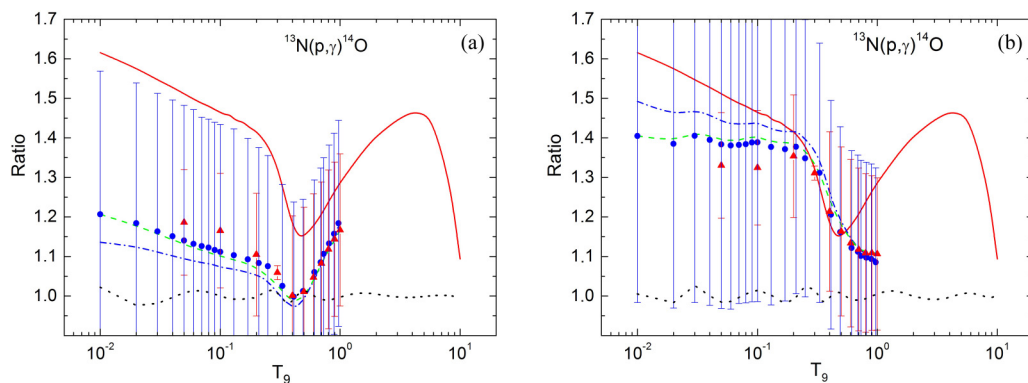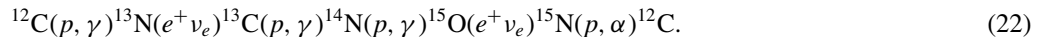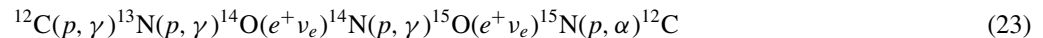

FIG. 6. The dependence of the ratio of the reaction rates on temperature. (a) The ratio of the reaction rate obtained in the present calculations and given in Refs. [15,21–23,26], correspondingly: NACRE II [26] (solid curve), Li *et al.* [15] (dash-dotted curve), Guo *et al.* [18] (dashed curve), Tang *et al.* [22] (circles with error bars), Magnus *et al.* [21] (triangles with error bars). The dotted curve is the ratio of the estimated speed to its approximation (21). (b) The ratios of the reaction rates obtained in the present calculations, Refs. [15,21–23] to the NACRE II [26] approximated with parameters from Table IV: present calculations (solid curve), Li *et al.* [15] (dashed curve), Guo *et al.* [18] (dash-dotted curve), Tang *et al.* [22] (circles with error bars), Magnus *et al.* [21] (triangles with error bars), correspondingly. The dotted curve corresponds to the ratio of NACRE II data and its approximation using the parameters from Table IV.

to Refs. [15,16,22,23], where the channel radius cutoff parameter is exploited. Concerning the *ANC*: we examined the cases with ANC_{min} and ANC_{max} and found ANC_{opt}, within the correlation of Γ_{tot}. Results in Refs. [15,16,22,23] are obtained based on the average *ANC* and do not examine or show the band variety on the cross sections or *S* factors within this very context.

VI. CNO AND HOT CNO CYCLES

Since the late 1930s, when von Weizsäcker [59] and Bethe [60] independently proposed sets of fusion reactions by which stars convert hydrogen to helium, it has been well established that the carbon-nitrogen-oxygen cycle is a mechanism for hydrogen burning in stars. The dominant sequence of reactions for this cycle is the following:

$$^{12}\text{C}(p, \gamma)^{13}\text{N}(e^+\nu_e)^{13}\text{C}(p, \gamma)^{14}\text{N}(p, \gamma)^{15}\text{O}(e^+\nu_e)^{15}\text{N}(p, \alpha)^{12}\text{C}. \tag{22}$$

The character of the nuclear burning is extremely temperature sensitive and, when the temperature is low enough, the hot carbon-nitrogen-oxygen cycle

$$^{12}\text{C}(p, \gamma)^{13}\text{N}(p, \gamma)^{14}\text{O}(e^+\nu_e)^{14}\text{N}(p, \gamma)^{15}\text{O}(e^+\nu_e)^{15}\text{N}(p, \alpha)^{12}\text{C} \tag{23}$$

starts. Since, at low T_9 temperatures, the ^{13}N$(p, \gamma)^{14}$O reaction in sequence (23) is competitive with the ^{13}N$(e^+\nu_e)^{13}$C decay in sequence (22), the formation and decay of ^{14}O becomes a major distinguishing feature of this higher-temperature cycle. Therefore, the stellar ^{13}N$(p, \gamma)^{14}$O reaction rate determines the order and the precise temperature of the conversion of the cold CNO cycle to the HCNO cycle and the waiting point in the cycle changes from ^{14}N to the ^{14}O and ^{15}O and the ^{13}N$(p, \gamma)^{14}$O reaction is a key process which determines this conversion.

One can say that the topic is hardly new, which is illustrated by the number of references on the *S* factor of the ^{13}N$(p, \gamma)^{14}$O reaction and the different reactions rates [15,16,19,21–23]. Reference [11] suggested the most consistent and accurate methodology for analyses of the temperature and density conditions for the HCNO cycle. Below we use this methodology along with our results for the ^{13}N$(p, \gamma)^{14}$O reaction rate and reanalyze the dependence of the lifetime against hydrogen burning via the ^{13}N$(p, \gamma)^{14}$O reaction as a function of temperature and find the temperature window and densities of a stellar medium at which the CNO cycle is converted to the hot CNO cycle. The reanalysis is extended for the stellar density dependence on temperature. Therefore, we use our results for the ^{13}N$(p, \gamma)^{14}$O reaction rate, follow Ref. [11], and find the temperature window and densities of a stellar medium at which the CNO cycle is converted to the hot CNO cycle. We can achieve the latter by comparing the ^{13}N$(p, \gamma)^{14}$O, ^{14}N$(p, \gamma)^{15}$O, and ^{12}C$(p, \gamma)^{13}$N reaction rates and the lifetime of nuclei against destruction by hydrogen burning.

The lifetime of isotopes in the stellar CNO cycle relative to the combustion of hydrogen one can be determined as follows [55,61]:

$$\tau = \frac{A_H}{\rho X_H} \frac{1}{N_A \langle \sigma_c v \rangle}, \tag{24}$$

where A_H is the atomic mass of hydrogen, X_H is the relative abundance of hydrogen by mass, ρ is the density of the stellar medium, and $N_A \langle \sigma_c v \rangle$ is the appropriate proton-capture reaction rate. Thus, as follows from Eq. (24), lifetime is determined precisely by the rate of the corresponding reaction. In our calculations, we use the ^{12}C$(p, \gamma)^{13}$N, ^{13}N$(p, \gamma)^{14}$O, and ^{14}N$(p, \gamma)^{15}$O reactions rates. In Fig. 7 the reaction rates

of the ^{13}N$(p, \gamma)^{14}$O, ^{14}N$(p, \gamma)^{15}$O, and ^{12}C$(p, \gamma)^{13}$N processes are shown, which are further used in the calculations of τ. For the ^{13}N$(p, \gamma)^{14}$O reaction we use results of the present calculations and data from Ref. [11], for the reaction ^{14}N$(p, \gamma)^{15}$O data Refs. [57] and [33] are used, while for the ^{12}C$(p, \gamma)^{13}$N we employed data [57], which are very close to data given in the NACRE II database [26]. Let us comment on the difference in the data for the ^{14}N$(p, \gamma)^{15}$O reaction (curves 3 and 5 in Fig. 7). In contrast to Ref. [57], in Ref. [33] the ^{14}N$(p, \gamma)^{15}$O reaction rate was calculated by taking into account the radiative capture of protons both in the GS of the ^{14}N nucleus and in all four excited bound levels. Such consideration allows one to describe experimental data for the astrophysical *S* factors of the proton radiative capture on ^{14}N to five excited states of the ^{15}O nucleus at excitation energies from 5.18 to 6.86 MeV, under the assumption that all five resonances are *D* scattering waves. The latter approach leads to a significant increase of the ^{14}N$(p, \gamma)^{15}$O reaction rate at temperatures $T_9 > 0.3$, which is indicated in Fig. 7.
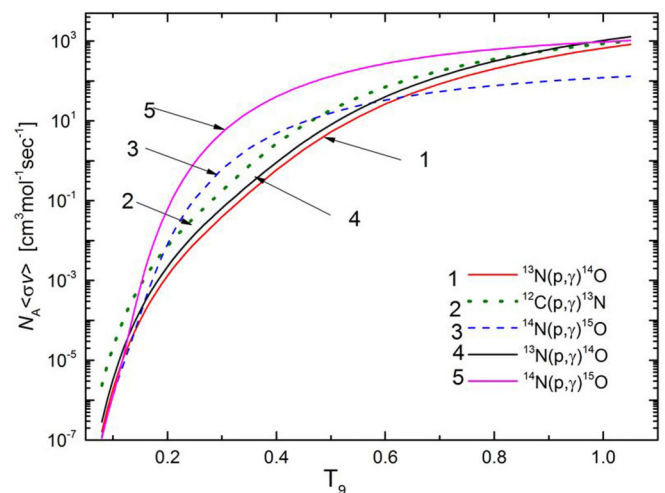
FIG. 7. The dependence of the reaction rates of the $N_A \langle \sigma_c v \rangle$ on temperature for the ^{12}C$(p, \gamma)^{13}$N, ^{13}N$(p, \gamma)^{14}$O, and ^{14}N$(p, \gamma)^{15}$O reactions. The data for curves 1, 2, and 3 are taken from Ref. [11], the data for curve 4 are from the present calculation, and the data for curve 5 are from Ref. [33].
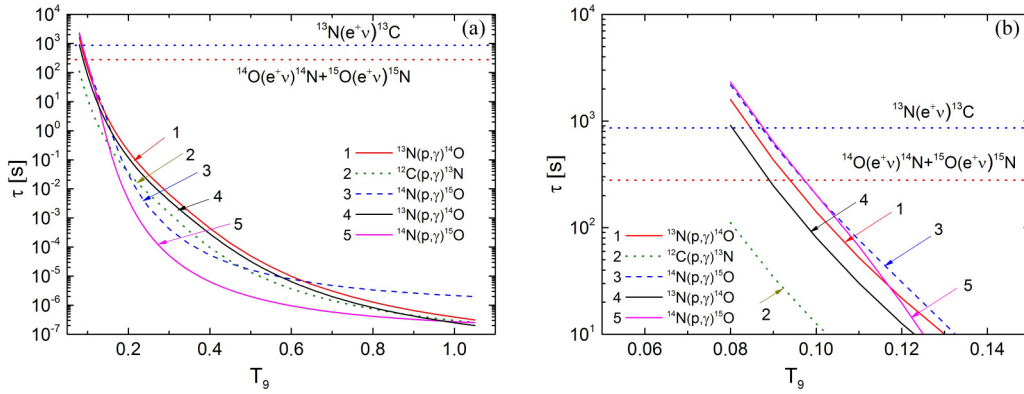
FIG. 8. Comparison of lifetime against hydrogen burning via the $^{12}C(p, \gamma)^{13}N$, $^{13}N(p, \gamma)^{14}O$, and $^{14}N(p, \gamma)^{15}O$ reactions as a function of temperature, and the ^{13}N, ^{14}O, and ^{15}O β-decay lifetimes for the temperature intervals (a) $0.08 < T_9 < 1.0$ and (b) $0.08 < T_9 < 0.14$.

To determine the astrophysical temperatures at which the CNO cycle is converted to the HCNO cycle, it is necessary to determine the $^{13}N(p, \gamma)^{14}O$ reaction rate as a function of temperature and compare it with one for the other processes. Using the reaction rates presented in Fig. 7, we calculate the dependence of the lifetime of isotopes produced in the processes $^{12}C(p, \gamma)^{13}N$, $^{13}N(p, \gamma)^{14}O$, and $^{14}N(p, \gamma)^{15}O$ on temperature. Following Ref. [11], in calculations we used for the hydrogen mass fraction $X_H = 0.77$ and the stellar density $\rho = 5 \times 10^3$ g/cm^3 [62].

The dependencies on temperature of the lifetime of isotopes produced in the processes are presented in Fig. 8. The data for the lifetime of radioactive isotopes are also presented in Fig. 8: $\tau_{^{13}N} = 863$ s for $^{13}N(e^+\nu_e)^{13}C$, $\tau_{^{14}O} = 102$ s for $^{14}O(e^+\nu_e)^{14}N$, and $\tau_{^{15}O} = 176$ s for $^{15}O(e^+\nu_e)^{15}N$. The analysis of the results presented in Fig. 8 shows that at $T_9 = 0.08$ the $^{13}N(p, \gamma)^{14}O$ and $^{13}N(e^+\nu_e)^{13}C$ reactions have equal lifetime. When the lifetime of ^{14}O isotope produced via $^{13}N(p, \gamma)^{14}O$ reaction will be less than the $^{13}N(e^+\nu_e)^{13}C$ decay lifetime, the reaction sequence changes to the hot CNO cycle. For these conditions in the CNO cycle the lifetimes of β^+-unstable systems such as ^{13}N and ^{15}O are long enough that proton capture can occur on these unstable nuclei before they undergo the β^+ decay.

The onset of the HCNO cycle occurs at $T_9 = 0.08$ when the rate of the slowest $^{13}N(p, \gamma)^{14}O$ reaction exceeds the $^{14}O(e^+\nu_e)^{14}N$ and $^{15}O(e^+\nu_e)^{15}N$ decay rates. Moreover, at $T_9 = 0.1$ the ratio of the $^{13}N(p, \gamma)^{14}O$ and $^{13}N(e^+\nu_e)^{13}C$ rates is 10.8, in contrast with Ref. [11], where this ratio is about 6. Therefore, at $T_9 = 0.1$ the reaction $^{13}N(p, \gamma)^{14}O$ is already ten times faster than the $^{13}N(e^+\nu_e)^{13}C$ decay, resulting in mass flow going via ^{14}O at the very onset of the HCNO cycle. The present result indicates that the HCNO cycle is turned on at the early stage of a nova explosion when the temperature is lower than reported in the earlier calculations of Refs. [11,18].

Our calculations lead to the temperature range $0.13 < T_9 < 0.97$, where the reaction rate of $^{14}N(p, \gamma)^{15}O$ is greater than the reaction rate of $^{13}N(p, \gamma)^{14}O$. The $^{13}N(p, \gamma)^{14}O$ reaction rate obtained in the present calculations leads to a temperature window which is much wider than that reported in Ref. [11]: $0.14 < T_9 < 0.64$. One should mention that the reaction rates for $^{13}N(p, \gamma)^{14}O$ in the present work and $^{14}N(p, \gamma)^{15}O$ in

Ref. [33] are obtained in the framework of the same theoretical approach.

Following Ref. [11], let us determine the dependence of the stellar medium density corresponding to the onset of the HCNO cycle on temperature as

$$\rho = \frac{A_H}{X_H(\tau_{^{14}N} + \tau_{^{15}N})} \frac{1}{N_A \langle \sigma_c v \rangle_{min}}, \quad (25)$$

where the smallest reaction rate $N_A \langle \sigma_c v \rangle_{min}$ includes the temperature dependence. An analysis of the density-temperature relationship allows us to determine the temperatures and densities at which the stellar CNO cycle is converted to the HCNO cycle. If the density and temperature of the stellar medium fall above the curve $\rho(T)$ on the density-temperature diagram, then the HCNO cycle occurs; otherwise, the CNO cycle operates.

The results of present calculations for the density-temperature dependence $\rho(T)$ along with results from Ref. [11] are shown in Fig. 9. The comparison of our calculations and results from Ref. [11] indicates that, in the same temperature range, the HCNO cycle operates at the lower den-
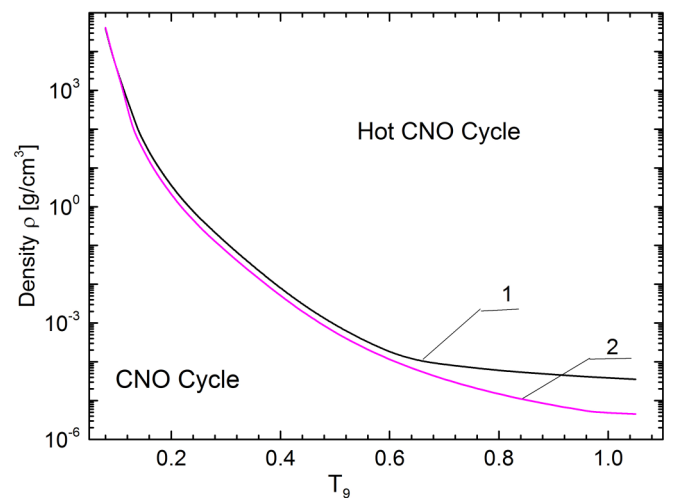

FIG. 9. Density and temperature range for the operation of the hot CNO cycle. Curves 1 shows the result from Ref. [11], curve 2 shows the present result.

sities of a stellar medium than in the case reported in Ref. [11]. Analysis of the results given in the density-temperature diagram in Fig. 9 demonstrate that, at the early stage of a nova explosion and in the temperature range $0.2T_9$–$0.4T_9$, the hot CNO cycle could be turned on at half the density of the stellar matter. The difference becomes more significant at $T_9 > 0.6$ and the HCNO cycle could be operated when, at $1T_9$, the stellar medium density becomes about 10 times less compared with that of Ref. [11], as can be seen from Fig. 9.

Reanalysis of the astrophysical S factor and reaction rate of the proton capture on the ^{13}N nucleus leads us to numerical differences with previous studies. These numerical differences bring us to a new temperature corridor for the conversion of stellar CNO cycle to the HCNO cycle. The small variation for the range of the HCNO window may lead to huge macroscopic consequences on the scale of astrophysical events. Thus, in supermassive stars at high temperature, the ignition of the hot CNO cycle can occur at much lower densities, generating sufficient energy which can affect the collapse of very massive stars at the end of their life cycle.

VII. CONCLUSION

We briefly summarize our results. We have employed the modified potential cluster model to describe the ^{13}N$(p, \gamma)^{14}$O reaction at astrophysical energies and the influence of the width of the first p ^{13}N resonance on the astrophysical S factor. At energies of 30–70 keV, the S factor remains almost constant with the average value of 8.4(2) keV b, thereby determining its value at zero energy, which is determined by the potential of S-wave scattering. The values of the $S(0)$ factor of 7.0(2) to 8.4(2) keV b are listed in Table I for three options of potentials, which correspond to three different values of energies for resonance in the S scattering wave. The potentials of the S wave, leading to the correct resonance width for different resonance energies, do not allow us to obtain the value of the S factor, which would be consistent with previous results. Only a decrease in the resonance width to 22–26 keV leads to an S factor of the order of 5 keV b, which is consistent with the upper limit of the results from Ref. [26] and the results of other works such as Refs. [16,22,23]. Thus, an accurate determination of the width is crucial. Our results demonstrate that contributions of the $M1$ and $E2$ transitions in the S factor are negligible at energies $E < 1$ MeV, but are significant at high energies. At the resonance energy, the S factor reaches 2.4 MeV b, which is in a good agreement with the results of previous studies. Using the MPCM capabilities, it was shown that the values of the astrophysical S factor for the ^{13}N$(p, \gamma)^{14}$O reaction at ultralow energies depends strongly on the $^3S_1$ resonance parameters.

Based on the potentials for the S scattering wave, consistent with the energy and widths of the first resonance, the ^{13}N$(p, \gamma)^{14}$O reaction rate was calculated and a simple analytical approximation for the reaction rate was proposed. The inclusion of resonances at 1.981, 3.117, and 5.123 MeV practically does not affect the reaction rate, although the contributions of resonances are clearly visible when calculating the S factor. The reason for such a weak influence is their small widths and relatively large resonance energies. Results of our calculations for the ^{13}N$(p, \gamma)^{14}$O reaction rate provide the contribution to the steadily improving reaction-rate libraries.

A precise knowledge of a cross section of the proton radiative capture on ^{13}N isotope at low energy is important because it plays a key role in the HCNO cycle, due to the proton capture rate on ^{13}N at temperature range of $0.05T_9$–$1.0T_9$ can become of the same order or larger than the ^{13}N$(e^+\nu_e)^{13}$C decay rate. Our calculations show that, at $T_9 = 0.1$, the ratio of the ^{13}N$(p, \gamma)^{14}$O rate to the ^{13}N$(e^+\nu_e)^{13}$C rate is 10.8.

In the context of the CNO cycle scenario, our calculations of the ^{13}N$(p, \gamma)^{14}$O and results for the other bottleneck ^{14}N$(p, \gamma)^{15}$O reaction [33], together with the NACRE II data [26] for the ^{12}C$(p, \gamma)^{13}$N process, show that, in the temperature window $0.13 < T_9 < 0.97$, where the reaction rate of ^{14}N$(p, \gamma)^{15}$O is greater than the reaction rate of ^{13}N$(p, \gamma)^{14}$O, the CNO cycle converts to the HCNO cycle. The present result indicates that the HCNO cycle is turned on at the early stage of a nova explosion at the temperature $T_9 = 0.08$. Therefore, the significant mass flow through ^{14}O nuclei begins to occur at the temperature $T_9 = 0.08$. Our calculations show that, at this temperature, the ^{13}N$(p, \gamma)^{14}$O reaction rate and the decay rate of the ^{13}N$(e^+\nu_e)^{13}$C process are equal.

Our results demonstrate that, at the early stages of a nova explosion, at temperatures of about $0.1T_9$, and at the late stages of evolution of supermassive stars at temperatures of about $1T_9$, the ignition of the hot CNO cycle could occur at much lower densities of a stellar medium.

Therefore, at the temperature and density of a stellar medium such as the conditions in a nova explosion and very massive stars, hydrogen burning occurs at temperatures $0.01T_9$–$1.0T_9$. For these conditions in the CNO cycle, the lifetimes of β^+-unstable systems such as ^{13}N and ^{15}O are long enough that proton capture can occur on these unstable nuclei before they undergo β^+ decay.

[1] E. Wiescher, J. Görres, E. Uberseder, G. Imbriani, and M. Pignatari, Annu. Rev. Nucl. Part. Sci. **60**, 381 (2010).

[2] M. Wiescher, F. Käppeler, and K. Langanke, Annu. Rev. Astron. Astrophys. **50**, 165 (2012).

[3] C. R. Brune and B. Davids, Annu. Rev. Nucl. Part. Sci. **65**, 87 (2015).

[4] M. Wiescher *et al.*, Nucl. Phys. A **349**, 165 (1980).

[5] C. A. Bertulani and A. Gade, Phys. Rep. **485**, 195 (2010).

[6] P. Decrock, Th. Delbar, P. Duhamel, W. Galster, M. Huyse, P. Leleux, I. Licot *et al.*, Phys. Rev. Lett. **67**, 808 (1991).

[7] P. Decrock, M. Gaelens, M. Huyse, G. Reusen, G. Vancraeynest, P. Van Duppen *et al.*, Phys. Rev. C **48**, 2057 (1993).

[8] Th. Delbar, W. Galster, P. Leleux, I. Licot, E. Lienard, P. Lipnik *et al.*, Phys. Rev. C **48**, 3088 (1993).

[9] T. E. Chupp, R. T. Kouzes, A. B. McDonald, P. D. Parker, T. F. Wang, and A. Howard, Phys. Rev. C **31**, 1023 (1985).

[10] P. B. Fernandez, E. G. Adelberger, and A. Garcia, Phys. Rev. C **40**, 1887 (1989).

[11] M. S. Smith, P. V. Magnus, K. I. Hahn, R. M. Curley, P. D. Parker, T. F. Wang *et al.*, Phys. Rev. C **47**, 2740 (1993).

[12] T. Motobayashi *et al.*, Phys. Lett. B **264**, 259 (1991).

[13] J. Kiener *et al.*, Nucl. Phys. A **552**, 66 (1993).

[14] G. Baur and H. Rebel, J. Phys. G **20**, 1 (1994).

[15] Z. H. Li *et al.*, Phys. Rev. C **74**, 035801 (2006).

[16] W. Liu *et al.*, Int. J. Mod. Phys. E **15**, 1899 (2006).

[17] R. J. Charity, K. W. Brown, J. Okolowicz, M. Ploszajczak, J. M. Elson, W. Reviol *et al.*, Phys. Rev. C **100**, 064305 (2019).

[18] G. J. Mathews and F. S. Dietrich, Astrophys. J. **287**, 969 (1984).

[19] K. Langanke, O. S. Van Rogsmalen, and W. A. Fowler, Nucl. Phys. A **435**, 657 (1985).

[20] C. Funck and K. Langanke, Nucl. Phys. A **464**, 90 (1987).

[21] P. V. Magnus, E. G. Adelberger, and A. Garcia, Phys. Rev. C **49**, R1755(R) (1994).

[22] X. Tang, A. Azhari, C. Fu, C. A. Gagliardi, A. M. Mukhamedzhanov, F. Pirlepesov, L. Trache *et al.*, Phys. Rev. C **69**, 055807 (2004).

[23] B. Guo and Z. H. Li, Chem. Phys. Lett. **435**, 65 (2007).

[24] J. T. Huang, C. A. Bertulani, and V. Guimarães, At. Data Nucl. Data Tables **96**, 824 (2010).

[25] C. Angulo *et al.*, Nucl. Phys. A **656**, 3 (1999).

[26] Y. Xu, K. Takahashi, S. Goriely *et al.*, Nucl. Phys. A **918**, 61 (2013).

[27] F. Ajzenberg-Selove, Nucl. Phys. A **523**, 1 (1991).

[28] S. I. Sukhoruchkin and Z. N. Soroko, *Excited Nuclear States*, Sub. G. Suppl. I/25 A-F (Springer, Netherlands, 2016).

[29] S. B. Dubovichenko, *Radiative Neutron Capture* (Walter de Gruyter GmbH, Berlin, Boston, 2019).

[30] M. Wiescher and T. Ahn, Clusters in astrophysics, in *Nuclear Particle Correlations and Cluster Physics*, edited by Wolf-Udo Schröder (World Scientific, Singapore, 2017), Chap. 8, pp. 203–255.

[31] S. B. Dubovichenko, *Thermonuclear Processes in Stars and Universe*, 2nd English ed. (Scholar's Press, Saarbrucken, 2015).

[32] S. B. Dubovichenko, N. A. Burkova, A. V. Dzhazairov-Kakhramanov, R. Ya. Kezerashvili, Ch. T. Omarov, A. S. Tkachenko, and D. M. Zazulin, Nucl. Phys. A **987**, 46 (2019).

[33] S. B. Dubovichenko, N. A. Burkova, and A. V. Dzhazairov-Kakhramanov, Int. J. Mod. Phys. E **29**, 1930007 (2020).

[34] C. A. Barnes, D. D. Clayton, and D. N. Schramm, *Essays in Nuclear Astrophysics. Presented to William A. Fowler* (Cambridge University Press, New York, 1982).

[35] S. B. Dubovichenko and A. V. Dzhazairov-Kakhramanov, Nucl. Phys. A **941**, 335 (2015).

[36] V. G. Neudatchin, V. I. Kukulin, V. N. Pomerantsev, and A. A. Sakharuk, Phys. Rev. C **45**, 1512 (1992).

[37] O. F. Nemets, V. G. Neudatchin, A. T. Rudchik, Yu. F. Smirnov, and Yu. M. Tchuvil'sky, *Nucleon Association in Atomic Nuclei and the Nuclear Reactions of the Many Nucleon Transfers* (Naukova Dumka, Kiev, 1988) (in Russian).

[38] K. Wildermuth and Y. C. Tang, *A Unified Theory of the Nucleus* (Vieweg, Braunschweig, 1977).

[39] Y. C. Tang, M. LeMere, and D. R. Thompsom, Phys. Rep. **47**, 167 (1978).

[40] S. B. Dubovichenko and A. V. Dzhazairov-Kakhramanov, Russ. Phys. J. **52**, 833 (2009).

[41] V. G. Neudatchin and Yu. F. Smirnov, *Nucleon Associations in Light Nuclei* (Nauka, Moscow, 1969) (in Russian).

[42] V. I. Kukulin, V. G. Neudatchin, and Yu. F. Smirnov, Nucl. Phys. A **245**, 429 (1975).

[43] C. Itzykson and M. Nauenberg, Rev. Mod. Phys. **38**, 95 (1966).

[44] D. A. Varshalovich, A. N. Moskalev, and V. K. Khersonski, *Quantum Theory of Angular Momentum* (World Scientific, Singapore, 1988).

[45] A. S. Tkachenko, R. Ya. Kezerashvilic, N. A. Burkova, and S. B. Dubovichenko, Nucl. Phys. A **991**, 121609 (2019).

[46] F. Hammache *et al.*, Phys. Rev. C **82**, 065803 (2010).

[47] E. M. Tursunov, S. A. Turakulov, and P. Descouvemont, Phys. At. Nucl. **78**, 193 (2015).

[48] https://physics.nist.gov/cgi-bin/cuu/Value?mudjsearch2520 for=atomnuc!.

[49] http://cdfe.sinp.msu.ru/services/ground/NuclChart_release. html.

[50] F. Nichitiu, *Phase Shifts Analysis in Physics* (Acad. Publ., Romania, 1980).

[51] A. M. Mukhamedzhanov *et al.*, Nucl. Phys. A **725**, 279 (2003).

[52] G. R. Plattner and R. D. Viollier, Nucl. Phys. A **365**, 8 (1981).

[53] W. A. Fowler, G. R. Caughlan, and B. A. Zimmerman, Annu. Rev. Astron. Astrophys. **5**, 525 (1967).

[54] D. Baye and E. Brainis, Phys. Rev. C **61**, 025801 (2000).

[55] S. G. Ryan and A. J. Norton, *Stellar Evolution and Nucleosynthesis* (Cambridge University Press, New York, 2010).

[56] http://cdfe.sinp.msu.ru/exfor/index.php.

[57] G. R. Caughlan and W. A. Fowler, At. Data Nucl. Data Tables **40**, 283 (1988).

[58] X. Tang *et al.*, Phys. Rev. C **67**, 015804 (2003).

[59] C. F. von Weizsäcker, Phys. Z. **38**, 176 (1937).

[60] H. A. Bethe, Phys. Rev. **55**, 103 (1939).

[61] C. Rolfs and W. S. Rodney, *Cauldrons in the Cosmos* (University of Chicago Press, Chicago, 1988).

[62] M. Wiescher, J. Gorres, F.-K. Thielemann, and H. Ritter, Astron. Astrophys. **160**, 56 (1986).